BRILLOUIN SCATTERING FROM POROUS p-TYPE 6H SILICON CARBIDE

CHRISTOPHER K. YOUNG

Your file Votre référence
ISBN: 978-0-494-33465-2
Our file Notre référence
ISBN: 978-0-494-33465-2

BRILLOUIN SCATTERING FROM POROUS p-TYPE 6H SILICON CARBIDE

by

Christopher K. Young

A Thesis Submitted in Partial Fulfillment of
the Requirements for the Degree of

Master of Science

Department of Physics and Physical Oceanography
Memorial University

March, 2007

St. John's Newfoundland

Abstract

Brillouin scattering was used to study acoustic modes in porous silicon carbide (PSC). Six samples, with porosities varying from 30% to 58%, were studied. Initially the samples were coated with a 40 nm aluminum layer and two Brillouin peaks were found with frequency shifts that increased with increasing angle of incidence but that could not be classified as Rayleigh surface modes. Two of the samples were studied while in a near vacuum environment but it was found that this did not affect the resultant frequency shifts. 50% HCl was used to remove the aluminum coatings and each sample was found to have a Rayleigh surface mode, with velocities ranging from 2.8×10^3 m/s to 5.2×10^3 m/s. The velocities were compared to, and agree closely with, those theoretically determined using the Mori-Tanaka acoustic effective medium model for spherical and prolate spheroid pore shapes. Four of the samples also had a mode that could be due to a pseudo-surface mode, with velocities ranging from 4.6×10^3 m/s to 8.4×10^3 m/s. Each sample was also found to have a transverse and longitudinal bulk mode, with velocities ranging from 3.1×10^3 m/s and 5.3×10^3 m/s and from 5.5×10^3 m/s to 9.7×10^3 m/s respectively. The velocities were compared to, and agree closely with, those determined by using the Mori-Tanaka model for prolate spheroid pore shapes. Due to the optical transparency of the sample, the slow and fast transverse bulk modes and the longitudinal bulk mode of the sample's silicon carbide (SiC) substrate were also detected. The average velocity values for

these peaks were determined to be 7.2×10^3 m/s, 7.5×10^3 m/s, and 12.8×10^3 m/s respectively. Using the data that was collected a more accurate value for the shape factor could possibly be determined. As well, further analysis would allow for the determination of the elastic constants for the PSC layers.

Acknowledgments

I would like to thank my supervisors, Dr. Andrews and Dr. Clouter, for all of the help, direction, and seemingly limitless knowledge that they provided during the duration of this project. I would also like to thank Dr. Choyke, Dr. Devaty and their coworkers at the University of Pittsburgh for providing the samples that were studied in this paper, as well as for providing graphs of the Mori-Tanaka acoustic effective medium model which were compared with the experimental data. I would also like to thank Ania Polomska for all of the help that she provided at various stage of this project, including collecting a number of spectra that were presented in this paper. I would also like to thank all my family members, especially my fiancée, Janna, and my son, Zachary, for the support that they have shown while I was undertaking this project.

Contents

List of Tables

List of Figures

Chapter 1

Introduction

The only known compound of silicon and carbon is called silicon carbide (SiC), which is an indirect bandgap semiconductor [1]. Silicon carbide can crystallize into a large variety of polymorphs and there are more than 200 different polytypes [2]. All of these polymorphs and polytypes have the same one-to-one stoichiometry, and all have a nearest neighbor arrangement that is very similar [1]. A material is polymorphic if it is capable of having different crystal structures [3]. The staking sequence of a double layer is the difference between polytypes. A double layer consists of a layer of close-packed silicon atoms and a layer of closed-packed carbon atoms stacked with the silicon layer on top of the carbon layer. The successive double layers are stacked, one on top of the other, in a close-packed arrangement [4]. The polytypes that occur most commonly are 3C, 4H, 6H and 15R [2]. The notation used is called Ramsdell notation, where the number refers to the number of double layers before the layer sequence begins to repeat [2]; C means cubic, H means hexagonal, and

R means rhombohedral [5]. 3C is the only polytype with a cubic crystal structure, whereas there are about 70 polytypes that have a hexagonal crystal structure, and approximately 170 polytypes that have rhombohedral crystal structure [4]. Due to these various polytypes, the indirect fundamental bandgap can vary from 2.39 eV for 3C SiC to 3.26 eV for 4H SiC [2].

For a long time it has been known that SiC has outstanding thermal [6], electrical [6–8], chemical [4,8] and mechanical [4,7,8] properties. In particular, the electrical and mechanical properties of SiC are better than silicon (Si) in many ways [8]. SiC has a wider bandgap [4,6–10], higher thermal conductivity [4,6,7] higher breakdown field [4,6,7,9], higher melting point [7,9], and higher saturation electron drift velocity [6,7,9] when compared to that of Si. These properties make SiC a good choice for the creation of high-temperature, high-frequency and high-power electronic devices [4,6,7]. As well, a high elastic modulus [4,7] and a fracture toughness higher than that of Si [4], in combination with its large bandgap, has made SiC a good material for the fabrication of microsensors that would be suitable for operation in temperatures in excess of 600°C [4]. SiC has a high tensile strength that can be of importance in mechanical systems [7]. SiC also provides great potential for the production of sensors that can operate in harsh conditions due to its high radiation resistance [4] and chemical inertness [4,7,8]. According to [10], a variety of far ranging applications could be significantly improved due to the ability of SiC to function under extreme conditions. This includes saving energy in electric vehicles and in

public electric power distribution, creating more powerful microwave electronics for radar and communication, and creating controls and sensors for clean-burning, increasing fuel efficiency [10]. Also, optical devices such as UV photodiodes and blue light-emitting diodes made using SiC are in a state of extensive development [7].

Porous SiC (PSC) can be made by using electrochemical etching of crystalline SiC in hydrofluoric acid. This procedure is similar to the one used to create porous Si [6,7,11–15]. A porous structure propagates into the bulk of the crystalline material due to the electrochemical etch but the general profile of the sample's surface appears unchanged [14]. When SiC is electrochemically etched, the bonds between the atoms that SiC is composed of are broken [13]. It has been found that Si atoms are more likely to be removed during the etch, leaving the porous layer carbon enriched [10,11, 13]. Similar to the case of electrochemically etching Si, it is seen that, for SiC, at a certain thickness the fibers of SiC become resistant to further etching. This is due to a sharp increase in the fibers' resistance when it reaches a certain thickness [11, 14]. According to [15], hexagonal SiC can be used to create PSC that has a number of different morphologies which indicates that the pore propagation is anisotropic. These different morphologies could potentially be used to satisfy different applications [15].

PSC is known to exhibit photoluminescence [6, 9, 10, 12–14] and UV luminescence [6,7]. The photoluminescence observed was generally in the blue or blue-green part of the visible spectrum [6,9,10,14]. The photoluminescence from PSC has been found to have an intensity between one to two orders of magnitude greater than the

photoluminescence from the corresponding crystalline SiC [6,13]. The photoluminescence from PSC has been found to be mostly independent of the polytype of SiC that is used [6,14]. Luminescence from PSC was determined to not be due to quantum size effects but was suggested to be a surface related effect [9]. It is suggested in [10] that the photoluminescence is due to carriers that were created in the core or on the surface of the sample that are excited from the valence band to the impurity levels or conduction band, and which then relax to their original state and recombine with C-H bonds, giving off photons in the process. According to [12], it was found that the dendritic morphology has a stronger luminescence when compared to the fiber-like morphology. It should also be noted that PSC can also exhibit electroluminescence [6,12]. According to [6], electroluminescence has been found in the blue and UV parts of the electromagnetic spectrum.

The luminescence properties of PSC make it a good candidate for integrated optoelectronics, for example, optical devices such as light emitting diodes [6]. Also, the great mechanical properties of SiC combined with the luminescence properties of PSC make it a good option for optoelectronics and communications that could be used in harsh environments [10]. PSC films, in the form of self-supporting films and PSC layers supported on SiC substrates, have been gaining interest in the fields of bone tissue engineering [8,15], fuel cell fabrication [8,15] and protein dialysis [15]. One other potential use of PSC is as the replacement for semi-insulating polycrystalline Si, which is used in Si technology. For this particular application, the PSC would

need to have a high resistivity while also allowing a small flow of current [14].

There have been a small number of Brillouin light scattering experiments performed on SiC and an even smaller number of Brillouin light scattering experiments have been performed on PSC. Both Matsukawa et al. [16] and Murata et al. [17] did similar Brillouin light scattering studies on thin layers of SiC on Si substrates. These experiments were done on various thin films of different polytypes with thicknesses ranging from 4.6 to 7.4 nm. The modified Rayleigh wave velocities of the SiC films were compared to the Rayleigh wave velocities of Si to determine what effect the films would have. It was found that if the film had a hexagonal or mixed (hexagonal and cubic) polytype, then the modified Rayleigh wave velocity was very similar to the Rayleigh wave velocity for Si [16, 17]. If the film had a cubic polytype it was found that the modified Rayleigh wave velocity was about 30 m/s lower than the Rayleigh wave velocity for Si [16, 17]. Also, if the film was amorphous it was found that the modified Rayleigh wave velocity was lower than the Rayleigh wave velocity for Si. This data implies that cubic and amorphous thin SiC films stiffen the Si surface, whereas hexagonal and mixed thin SiC films have little effect on the Si surface.

Djemia et al. [4] did Brillouin light scattering studies on an monocrystalline 3C-SiC film and a polycrystalline 3C-SiC film, each of which were grown on Si substrates. The three independent elastic constants for the monocrystalline film were determined from the Brillouin spectra that were collected and these values agreed fairly well with theoretical determinations and with preliminary results from ongoing experiments.

The five independent elastic constants for the polycrystalline film were determined from the Brillouin spectra that were collected. These values agreed fairly well with values calculated by the Voigt and Reuss averaging procedures.

Kamitani et al. [18] performed Brillouin light scattering experiments on one 4H and three 6H SiC samples. In this experiment all five independent elastic constants for both 4H and 6H SiC were determined from the Brillouin spectra. Most of these values agreed well with previous calculated values except for C_{13}, which had not been previously determined by Brillouin light scattering or ultrasonic techniques.

Andrews et al. [19] performed Brillouin light scattering experiments on samples of 6H PSC that were coated with thin layers of aluminum. First, a crystalline sample covered with 70 nm of aluminum was studied and it was found to have a surface velocity of about 6000 m/s. Subsequently, a sample with a high but undetermined porosity and a 40 nm coating of aluminum was studied and it was found to have a surface velocity of about 2400 m/s. Also, a sample that had a porosity of about 50% and an aluminum layer of 50 nm on one half, 58 nm on the other half was studied. It was found that the surface velocity for the half with a 58 nm layer of aluminum was about 2850 m/s while the surface velocity for the half with a 50 nm layer of aluminum had a surface velocity of about 2600 m/s. This agreed with the expectation that at lower aluminum layer thicknesses the velocity would be lower, but not enough data was collected to determine the surface velocity if there was no aluminum layer present.

This thesis consists of an inelastic laser light scattering study of acoustic phonon

propagation in PSC. Studies were performed to determine the effect of aluminum layers on PSC samples as well as to determine if the surface and bulk mode velocities are dependent on the porosities of the samples.

Chapter 2

Theory

2.1 Brillouin Light Scattering

The interaction between electromagnetic radiation (e.g. visible light) and matter can result in a variety of scattering processes. This matter may be solid, gas or liquid, with the light being scattered by excitations and/or fluctuations of the various optical properties of the matter [20]. These fluctuations are caused in part by the propagation of thermally excited sound waves in the material [21]. When photons are incident on a solid they can be scattered by the atoms of which the solid is composed. If these photons exchange energy and momentum with lattice vibrations, *i.e.* phonons, the scattered photons can exit the solid with energy and momentum that is different compared to the incident photons [3]. The scattering of a photon can be thought of as the temporary absorption of an incident photon that occurs at the same instant as an electronic excitation of an atom. This process is followed by the de-excitation of the atom and the emission of a photon. Inelastic photon-phonon

scattering is accompanied by a change in the energy of both collision partners [3]. Brillouin light scattering is the scattering of light by acoustic phonons and, as such, can be compared to collisions in mechanics [22]. This means that the conservation of energy and momentum before and after scattering must be taken into account. The energy of a photon is $E = \hbar\omega$ and the momentum of a photon is $\mathbf{p} = \hbar\mathbf{k}$, where $\hbar$ is Planck's constant, ω is the angular frequency of the photon and $\mathbf{k}$ is the wavevector of the photon. Similarly, the energy of a phonon is $E = \hbar\Omega$, where Ω is the angular frequency of the phonons, and the momentum of a phonon is $\mathbf{p} = \hbar\mathbf{q}$, where $\mathbf{q}$ is the wavevector of the phonon. From this it can be seen that for the conservation of energy,

$$\hbar\omega_i = \hbar\omega_s \pm \hbar\Omega, \tag{2.1}$$

where ω_i and ω_s are the angular frequencies of the incident and scattered photons, respectively. It can also be seen that for the conservation of momentum,

$$\hbar\mathbf{k}_i = \hbar\mathbf{k}_s \pm \hbar\mathbf{q}, \tag{2.2}$$

where $\mathbf{k}_i$ and $\mathbf{k}_s$ are the wavevectors of the incident and scattered beams, respectively.

The two processes that occur in inelastic light scattering are phonon creation and phonon annihilation, and are illustrated in Figure 2.1. For phonon creation, the scattered photon has an angular frequency that is less than the incident photon's angular frequency. This is because some of the energy from the incident photon was used to create a phonon. Phonon annihilation is the opposite of this and it is found that the scattered photon's angular frequency is greater than the incident photon's

angular frequency due to the annihilation of a phonon. These two processes result in a spectrum with peaks that have a negative and a positive frequency shift relative to the incident laser frequency, and also account for the plus or minus sign in equations (2.1) and (2.2). The negative-frequency shifted peak is referred to as the Stokes line and the positive-frequency shifted peak is referred to as the anti-Stokes line [3].

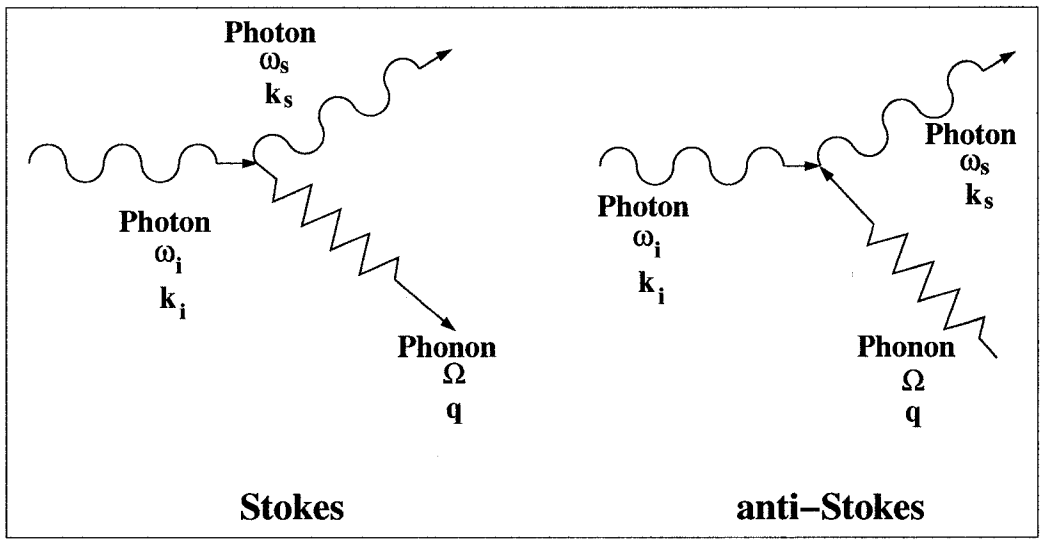

Figure 2.1: Stokes and anti-Stokes processes for inelastic light scattering [3].

There are two distinct mechanisms by which light can be scattered by acoustic waves. The first mechanism is called the bulk elasto-optic mechanism. In this mechanism, the incident light is scattered by the acoustic modulation of the dielectric constant of the matter. If the matter is a transparent solid and the optical wavevectors are real, then all of the components of the wavevectors are conserved. The

second mechanism is called the surface-ripple mechanism. With this mechanism, incident light is scattered by the dynamic acoustic deformation of the matter's surface, and only the wavevector component that is parallel to the surface is conserved by the scattered light [23]. Two basic types of acoustic modes can be probed via Brillouin light scattering because of the two mechanisms discussed above. They are known as bulk modes and Rayleigh-type surface modes, respectively.

It should be noted that scattered radiation undergoes a frequency broadening due to the finite lifetime of the excitation, τ_Q. If a matter excitation is exponentially damped, it is found that the line shape is Lorentzian with the full width at half maximum intensity, $\Delta\nu$, defined as

$$\Delta\nu = \frac{\Gamma_Q}{2\pi} = \frac{1}{2\pi\tau_Q} \tag{2.3}$$

where Γ_Q is the angular frequency linewidth [20].

2.1.1 Bulk Scattering

In solids it has been observed that elastic waves can have free and practically undamped propagation. The intensity of Brillouin scattering by these waves in transparent media is determined by their piezo-optic constants. For any direction in the bulk of a solid there are generally three different types of elastic waves, two transverse and one longitudinal wave, each with different velocities. This leads to the expectation that three pairs of Brillouin peaks will be observed when probing a crystalline solid [24]. From Equation (2.1) it can be seen that the shift in frequency between

the incident and scattered photons is equal to the frequency of the phonon. It is also known that

$$\Omega = v_p q, \tag{2.4}$$

where v_p is the phonon velocity in the bulk of the solid. The angular frequency of the phonon is about 1000 times smaller than the angular frequency of the incident light, therefore the assumption can be made that $\Omega << \omega_i$. From here it is seen that $k_i \simeq k_s$. It can now be shown from Figure 2.2 that

$$q = 2k_i \sin\frac{\psi}{2}, \tag{2.5}$$

where ψ is the angle between the incident photon and the scattered photon. Substituting Equation (2.5) into Equation (2.4) and using the fact that $k_i = \frac{2\pi n}{\lambda}$, it is found that

$$\Omega = \frac{4v_p n\pi}{\lambda}\sin\frac{\psi}{2}, \tag{2.6}$$

where n is the refractive index of the solid and λ is the wavelength of the incident light. For the backscattering configuration ($\psi = 180°$), Equation (2.6) becomes

$$\Omega = \frac{4v_p n\pi}{\lambda}. \tag{2.7}$$

2.1.2 Surface Scattering

Rayleigh surface waves are characterized by having displacement amplitudes primarily normal to the surface that decrease exponentially with increasing distance

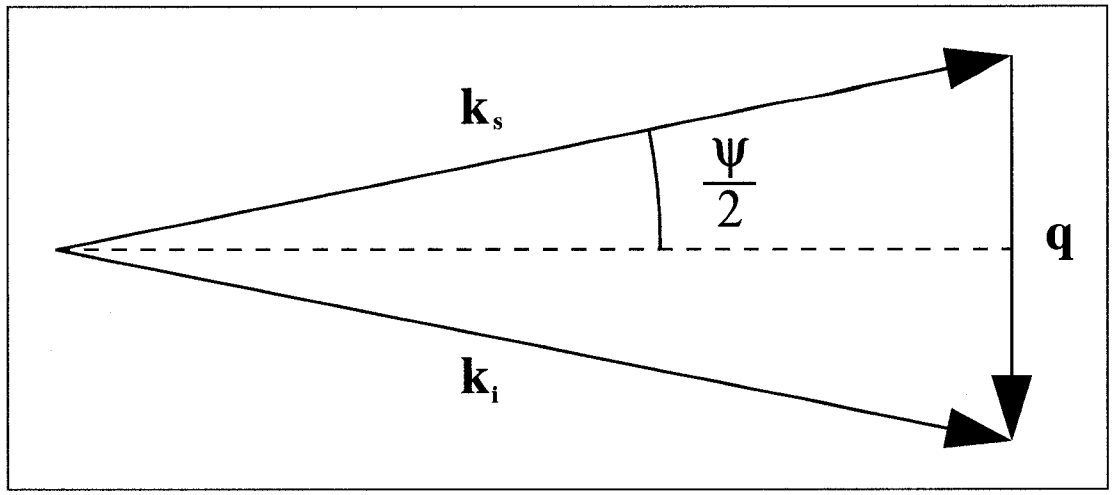

Figure 2.2: Brillouin scattering geometry where $\mathbf{k}_s$ is the wavevector of the scattered photon, $\mathbf{k}_i$ is the wavevector of the incident photon, $\mathbf{q}$ is the wavevector of the phonon, and ψ is the angle between the incident photon and the scattered photon [22].

from the medium's surface [25]. According to [26], taking Equation (2.2) and using Figure 2.3 it is seen that

$$q_S^{\parallel} = k_i \sin\theta_i \pm k_s \sin\theta_s, \tag{2.8}$$

and

$$q_S^{\perp} = n(k_i \cos\theta_i' \pm k_s \cos\theta_s'), \tag{2.9}$$

where $q_S^{\parallel}$ and $q_S^{\perp}$ are the parallel and perpendicular components of the surface phonon wavevector respectively, θ_i is the angle between the surface normal and the incident photon, θ_s is the angle between the surface normal and the scattered photon, θ_i' is the angle between the surface normal and the refracted incident photon, and θ_s' is the angle between the surface normal and the refracted scattered photon. For surface scattering, Equation (2.9) breaks down because the surface phonon amplitude decreases to zero

a small distance from the surface, therefore $q_S = q_S^{\parallel}$ so it can be shown that

$$q_S = k_i \sin\theta_i \pm k_s \sin\theta_s. \tag{2.10}$$

It is known that $\Omega << \omega_i$ and that $k_i \simeq k_s$. Also, using the fact that in a backscattering configuration $\theta_i \simeq \theta_s$, it can be found that

$$q_S = 2k_i \sin\theta_i. \tag{2.11}$$

As in the bulk case, $\Omega_S = v_S q_S$, where v_S is the surface phonon velocity, however ω_i will differ from the bulk case because, at the surface of the solid, $k_i = \frac{2\pi}{\lambda}$. Now using Equation (2.11) it is seen that

$$\Omega_S = \frac{4\pi v_S}{\lambda} \sin\theta_i. \tag{2.12}$$

Equations (2.7) and (2.12) are Brillouin equations from which acoustic mode velocities can be determined once acoustic frequency shift values are known.

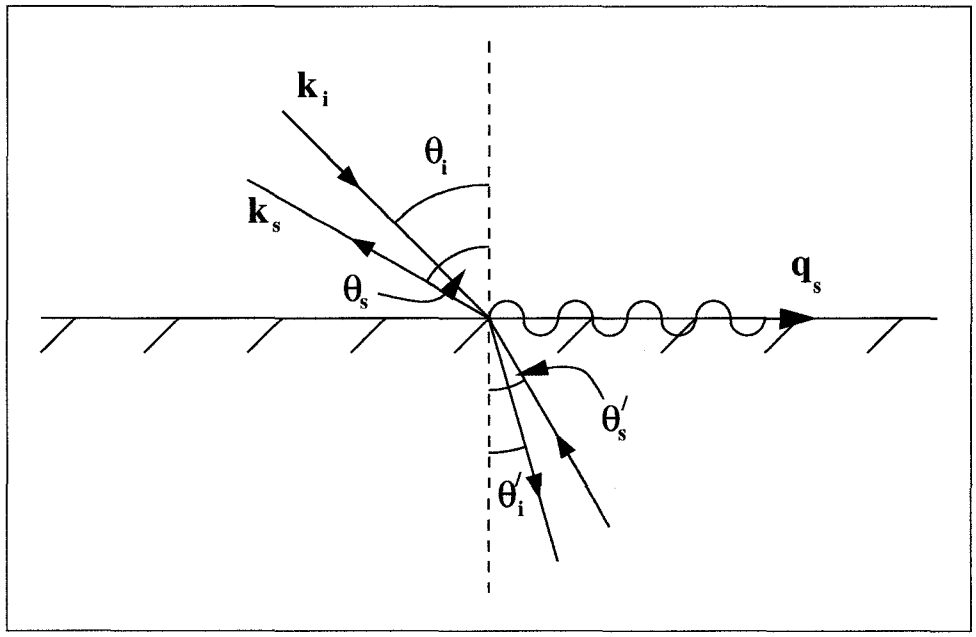

Figure 2.3: Light scattering from a surface where $\mathbf{k}_s$ is the wavevector of the scattered photon, $\mathbf{k}_i$ is the wavevector of the incident photon, $\mathbf{q}_s$ is the wavevector of the surface phonon, θ_i is the angle between the surface normal and the incident photon, θ_s is the angle between the surface normal and the scattered photon, θ_i' is the angle between the surface normal and the refracted incident photon, and θ_s' is the angle between the surface normal and the refracted scattered photon [26].

Chapter 3

Methods and Materials

3.1 Experimental Setup

For Brillouin scattering, most of the acoustic modes have frequencies that lie within a few tens of gigahertzs from the excitation source [27]. A Fabry-Perot interferometer can detect these low frequency modes making it the ideal instrument for Brillouin light scattering studies.

The setup that was used in this experiment is illustrated in Figure 3.1. A Coherent Verdi-V2 solid-state, diode-pumped, frequency-doubled Nd:YVO_4 single mode laser produces vertically polarized light at a wavelength of 532 nm. The laser power was set to 2 W and that power was reduced by a variable neutral density filter. A beam steerer raised the height of the beam while a filter further reduced the power of the beam. The beam passes through an aperture and a half-wave plate acts to rotate the plane of polarization of the light by 90 degrees, resulting in horizontally polarized light which was then incident on a partial reflector. The reflected beam is used as

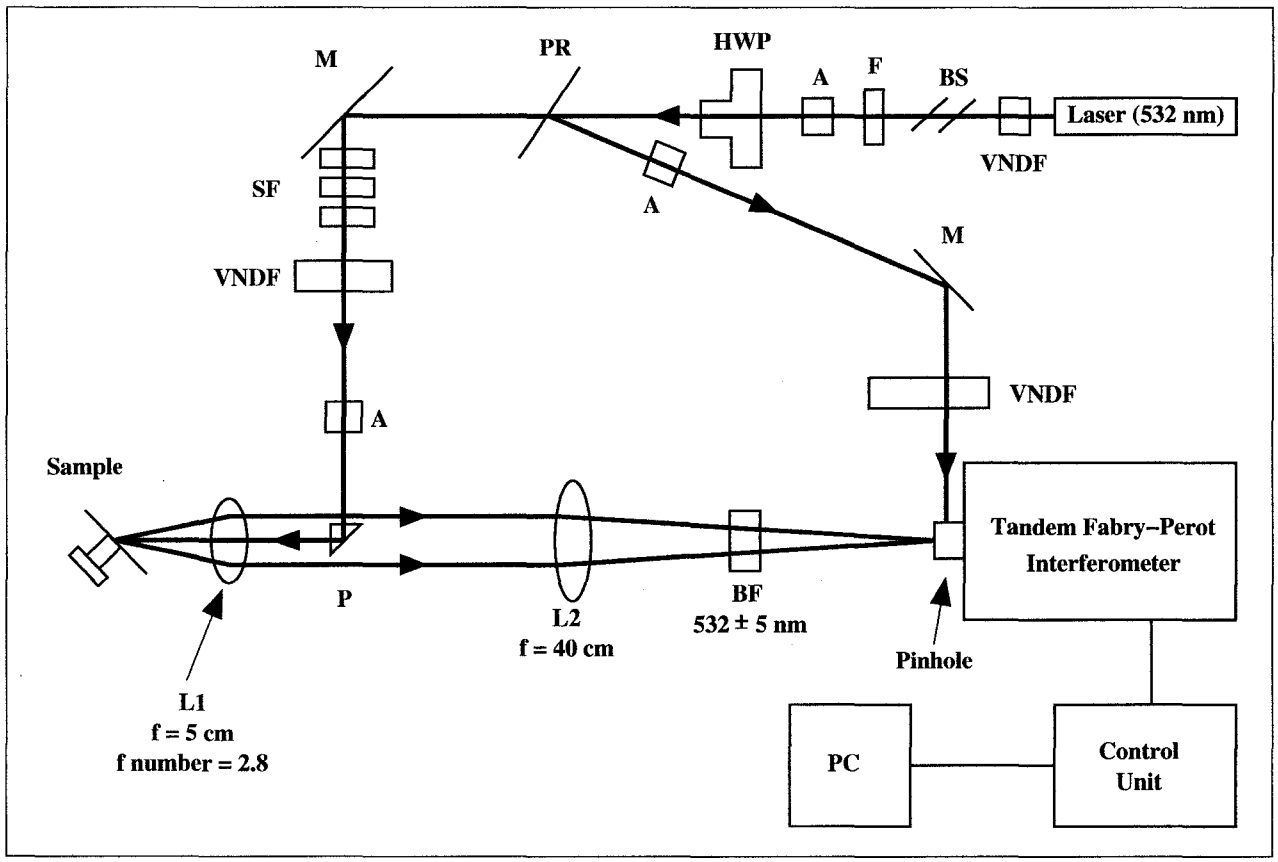

Figure 3.1: Experimental setup where VNDF is a variable neutral density filter, F is an absorbing filter, HWP is a half-wave plate, PR is a partial reflector, M is a mirror, SF is a set of absorption filters, A is an aperture, BS is a beam-steerer, L1 is a lens with a focal length of 5 cm, L2 is a lens with a focal length of 40 cm, BF is a band-pass filter, and P is a prism.

a reference beam and is directed to a tandem Fabry-Perot interferometer (discussed later) by a front-surface mirror. A variable neutral density filter permits adjustment of the reference beam intensity. This reference beam is used to maintain the mirror alignment (parallelism) of the Fabry-Perot interferometer and prevents saturation of the photomultiplier tube while the Fabry-Perot interferometer is scanning over the part of the spectrum that contains the intense elastically scattered light.

The beam transmitted by the partial reflector continues on to a front-surface mirror that deviates its path by 90°. It then passes through a set of filters, a variable neutral density filter and an aperture and is internally reflected by a prism to continue parallel to its original path. The beam is focused onto the sample using a lens with a focal length of 5 cm and an f-number of 2.8. Some of the light that is scattered by the sample is collected and collimated by the same lens that focused the incident beam. This light is subsequently focused by a lens with a focal length of 40 cm onto the input pinhole of a tandem Fabry-Perot interferometer, TFP-1, made by JRS Scientific Instruments. It is important to note the bandpass filter that is located between the second lens and the input pinhole. This filter only passes light that has a wavelength lying in the range of 532 ± 5 nm, and is intended in particular to block any Raman scattering that may be present.

The tandem Fabry-Perot interferometer (see Figure 3.2) has two Fabry-Perot interferometers in series and the light passes through each interferometer three times. A Fabry-Perot interferometer consists of 2 mirrors that are highly parallel and are

partially reflective [28]. These mirrors are separated by a distance, d, and by changing this distance using piezoelectric stacks, a Fabry-Perot interferometer acts as a tunable wavelength filter and, therefore, a tunable frequency filter [29].

Fabry-Perot interferometers work on the concept of interference due to multiple reflections. The transmission coefficient for a Fabry-Perot interferometer with light incident perpendicular to the first mirror is

$$T = \frac{T_{\max}\left(1-\rho^2\right)^2}{\left(1-\rho^2\right)^2 + 4\rho^2 \sin^2\left(\frac{2\pi d}{\lambda}\right)} \tag{3.1}$$

where $T_{\max}$ is the maximum transmission, d is the mirror separation, ρ is the reflection coefficient, and λ is the wavelength of the light [30]. Collimated light that is normally incident on a Fabry-Perot interferometer will be transmitted through the mirrors if it satisfies the relationship

$$m\lambda = 2d \tag{3.2}$$

where m is the order of a bright fringe and is an integral value [30]. The free spectral range of a Fabry-Perot interferometer is the separation of adjacent transmission peaks and is given (in Hz) by

$$FSR = \frac{c}{2d} \tag{3.3}$$

where c is the speed of light [30]. The quality of a Fabry-Perot interferometer can be determined by a dimensionless factor called the finesse, which is the ratio of the free spectral range to the instrumental width, and is given as

$$F = \frac{FSR}{\Delta\nu} \tag{3.4}$$

where $\Delta\nu$ is the instrumental width, which is also known as the resolution, and is the minimum spectral width that can be resolved by the instrument [31]. The finesse is determined primarily by the mirror reflectivity and flatness [32].

Passing light multiple times through a single Fabry-Perot interferometer greatly increases the contrast of that Fabry-Perot interferometer [33]. Using two Fabry-Perot interferometers in series provides the means of increasing the free spectral range while maintaining a fixed resolution, therefore increasing the finesse. Using a system where the spacings of the two mirrors, L_1 and L_2, are similar, but not the same, is most useful. Both Fabry-Perot interferometers need to satisfy Equation (3.2), therefore it is seen that

$$2L_1 = p\lambda \quad \text{and} \quad 2L_2 = q\lambda \tag{3.5}$$

where p and q are integral values. The neighboring transmission peaks for each Fabry-Perot interferometer will not perfectly overlap when L_1 and L_2 are similar, meaning there will be smaller adjacent peaks when compared to single Fabry-Perot interferometers [32]. A frequency spectrum can be obtained from a Fabry-Perot interferometer by varying the mirror spacing and, for a tandem Fabry-Perot interferometer, both mirror spacings must be simultaneously varied. From Equation (3.5) it can be seen that the changes in mirror spacings, δL_1 and δL_2, must satisfy

$$\frac{\delta L_1}{\delta L_2} = \frac{L_1}{L_2}. \tag{3.6}$$

To satisfy both the condition that the mirror spacings be similar and that the changes

in the mirror spacings follow Equation (3.6), one mirror from each Fabry-Perot interferometer was mounted on a translation stage while the other mirrors were mounted on angular orientation devices that were separate from the translation stage. The first Fabry-Perot interferometer was set to lie with its axis in the direction of the translation stages movement and the second Fabry-Perot interferometer was set so that its axis lies at an angle θ to the translation stages movement. This setup allows for both statically and dynamically stable synchronization of both mirror spacings. The mirrors are positioned such that when the translation stage has moved completely to the left both sets of mirrors would be in simultaneous contact. This means that if the mirrors are not in contact the mirror spacings are L_1 and $L_2 = L_1 \cos\theta$. This also guarantees that for a stage translation of δL_1 the mirror spacings change by δL_1 and $\delta L_2 = \delta L_1 \cos\theta$. With these spacing values both requirements are fulfilled.

The tandem Fabry-Perot interferometer is schematically illustrated in Figure 3.2. Light enters through the pinhole, passes through an aperture, and strikes mirror 1. A lens acts to collimate the beam and mirror 2 directs the light towards the first Fabry-Perot interferometer. When the light exits the first Fabry-Perot interferometer it passes through an aperture and mirror 3 directs the light towards the second Fabry-Perot interferometer. After the light exits the second Fabry-Perot interferometer the light strikes a 90° prism where it is reflected downwards and returns parallel to itself. The light then passes through the second Fabry-Perot interferometer, strikes mirror 3, passes through an aperture and the first Fabry-Perot interferometer, and strikes

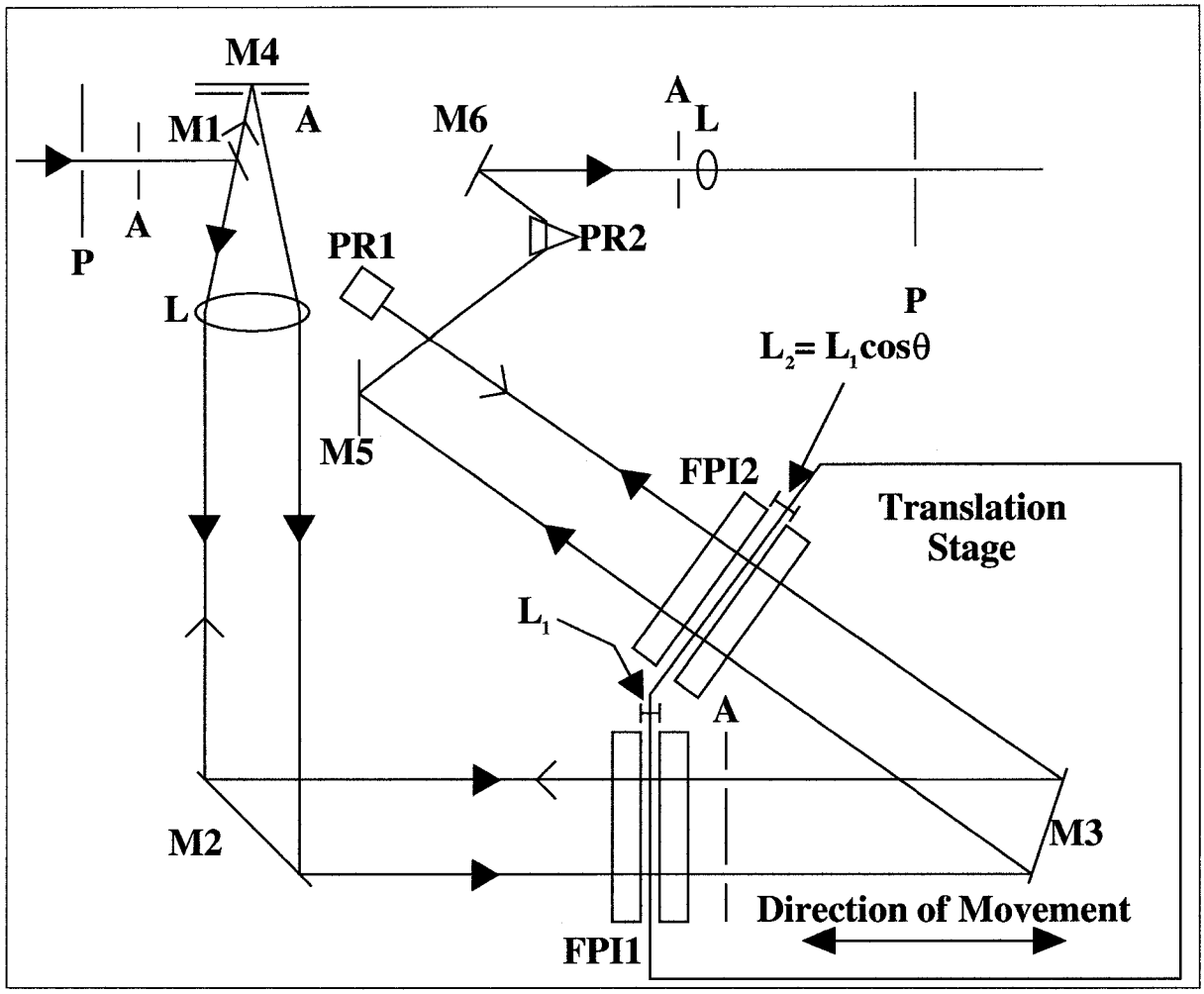

Figure 3.2: Tandem Fabry-Perot Interferometer where P is a pinhole, A is an aperture, M1, M2, M3, M4, M5 and M6 are mirrors, L is a lens, FPI1 and FPI2 are Fabry-Perot interferometers, PR1 is a 90° prism, and PR2 is a prism [32].

mirror 2. The lens focuses the light through an aperture onto mirror 4. The light does not strike mirror 1 due to the vertical displacement caused by the 90° prism. The light reflects off of mirror 4 and is collimated by the lens. The light subsequently travels through both Fabry-Perot interferometers once more before striking mirror 5. The light passes through the prism and is reflected off of mirror 6, passes through an aperture, lens and pinhole to then enter the photomultiplier [32]. Figure 3.2 also shows the translation stage and how the mirrors of the two Fabry-Perot interferometers are mounted in relation to it. The interferometer is run by a control unit which maintains the parallelism of the mirrors and also minimizes the cavity length changes (other than those desired, *i.e.* scanning). The information from the interferometer is then passed on to a computer where it is displayed.

3.2 Drying System

To ensure that there was no excess water on the samples or in the pores of the samples, a drying system was constructed. This setup is illustrated in Figure 3.3. The setup consists of a dewar, a ceramic heater and a glass container. The ceramic heater is connected to a variable resistance power supply and is near the bottom of the dewar. On the bottom of the glass container there is aluminum foil to help with heat conduction and a thermometer is in contact with the aluminum foil near the sample to monitor the temperature of the sample. The glass container is connected to a vacuum pump so that a majority of the air in the container can be removed.

The drying system was designed to be able to heat a sample to a temperature of approximately 150°C for a period of time of about 5 hours to try and remove any water that may be in or on the sample.

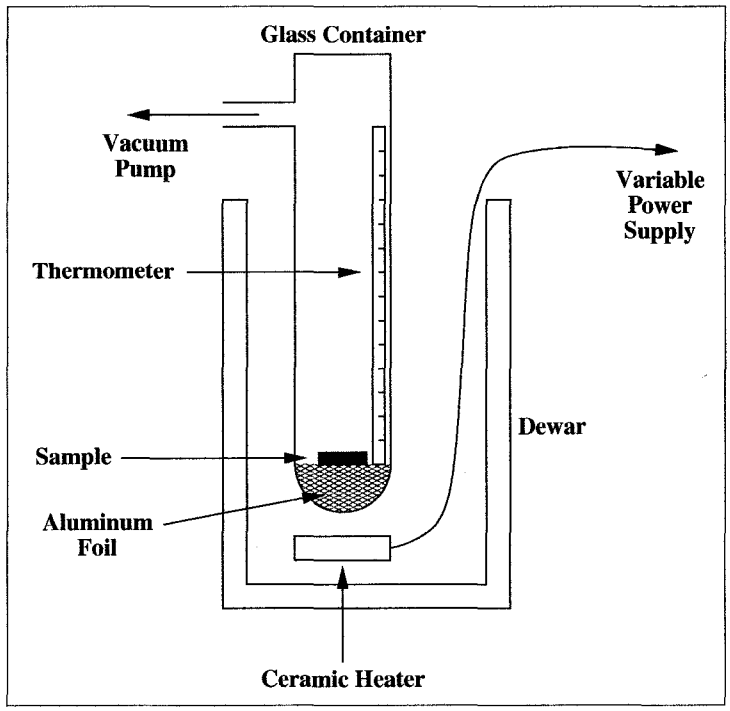

Figure 3.3: Drying Setup.

3.3 Gas Handling System

To minimize the environmental effects on the samples after having been dried, a gas handling system was used. This system is illustrated in Figure 3.4 and is comprised of a pressure gauge, two valves and a special sample holder. The system

was designed in such a way that a sample could be studied in near vacuum or in any gas atmosphere at any pressure up to approximately atmospheric pressure.

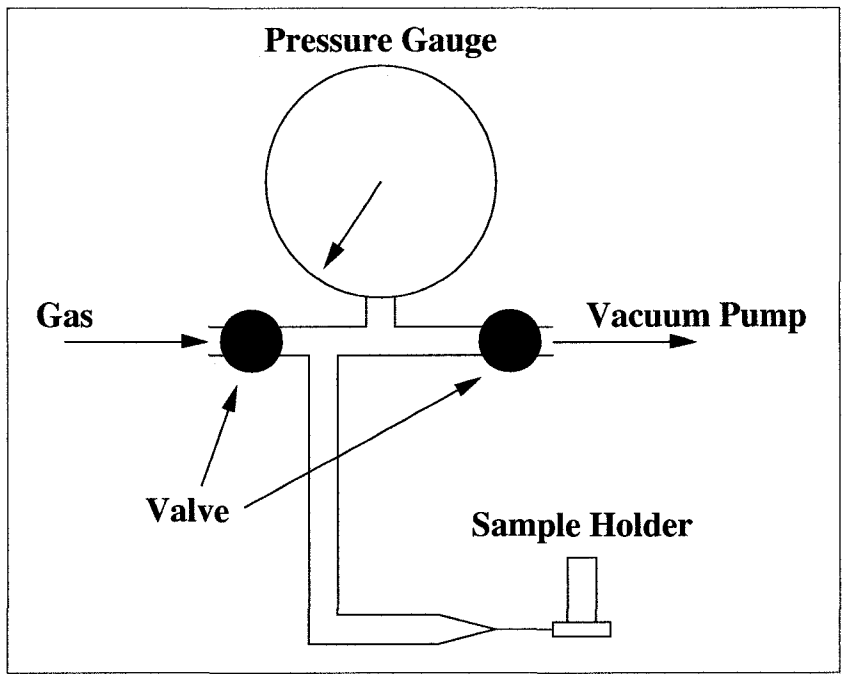

Figure 3.4: Gas Handling System.

3.4 Sample Preparation

All samples were made by W. J. Choyke and coworkers at the University of Pittsburgh using a method similar to that described in [8]. Wafers of p-type 6H silicon carbide, doped to approximately 7×10^{18} cm^{-3}, were electrochemically etched in an electrolytic solution that consists of 10% hydrofluoric acid and 5% ethanol. This

process creates PSC films that are supported on SiC substrates. The samples have an etched area of ~ 0.35 cm^2, were etched 3.2° off of the c-axis and have a branched morphology. All of the samples originally had an aluminum coating with a thickness of approximately 40 nm. The aluminum was thermally evaporated onto the samples. In an attempt to prevent the aluminum from entering the pores, the thermal evaporations were done with the normal of the samples surface at an angle of 75° to the vertical axes of the evaporator. Table 3.1 shows the sample name, current density, etching time, estimated porous layer thickness and estimated volume porosity of the samples. The volume porosities were estimated using the equation,

$$VP = \frac{m_1 - m_2}{\rho A d}, \tag{3.7}$$

where VP is the estimated volume porosity, ρ is the density of SiC, A is the etched area, d is the estimated porous layer thickness, m_1 is the mass of the sample before the etch and m_2 is the mass of the sample after the etch.

Table 3.1: Sample Information

Sample Name	Current Density (mA/cm^2)	Etching Time (Hours)	Estimated Porous Layer Thickness (μm)	Estimated Volume Porosity
BQ0423-15 #3	6	3	30	$39 \pm 8\%$
BQ0423-15 #4	32	0.75	28	$56 \pm 11\%$
BQ0423-15 #5	16	1.5	28	$58 \pm 12\%$
BQ0423-15 #6	2	6	26	$30 \pm 6\%$
BQ0423-15 #9	4	3	22	$35 \pm 7\%$
BQ0423-15 #10	8	3	28	$57 \pm 11\%$

Chapter 4

Results and Discussion

4.1 Aluminum Coated Samples

Due to the optical transparency of SiC, aluminum coatings were used to minimize the penetration depth of the laser light in an attempt to observe any surface modes from the samples. The Brillouin light scattering experiments on the aluminum coated samples were performed in air at atmospheric pressure under ambient conditions, except for samples BQ0423-15#5 and BQ0423-15#10 which were performed in near vacuum, using a backscattering configuration. BQ0423-15#5 and BQ0423-15#10 were studied in a near vacuum environment because it was believed that moisture in the air would damage the aluminum coatings. It was later found that spectra collected in air were qualitatively the same as spectra collected at near vacuum, meaning that studying the samples in a near vacuum environment was unnecessary. The aluminum coatings were approximately 40 nm in thickness. These samples have porosities ranging from 30% to 58% (see Table 3.1). It was found that a beam power

of a few tens of milliwatts was sufficient to provide a signal from the samples. It should also be noted that the samples were not damaged by being subjected to these beam powers. The FSR was set to observe the acoustic peaks and was typically set to 50 GHz.

4.1.1 BQ0423-15#3 ($\sim$ 39% Porosity)

Figure 4.1 shows Brillouin spectra collected from BQ0423-15#3 (aluminum coated) at angles of incidence ranging from 20° to 70° at 10° intervals, where the central peak, which has an assigned frequency shift of 0 GHz, is due to elastic scattering. These spectra were taken with a beam power of approximately 50 mW and an FSR of 50 GHz. Using OriginLab OriginPro analysis software it was determined that there

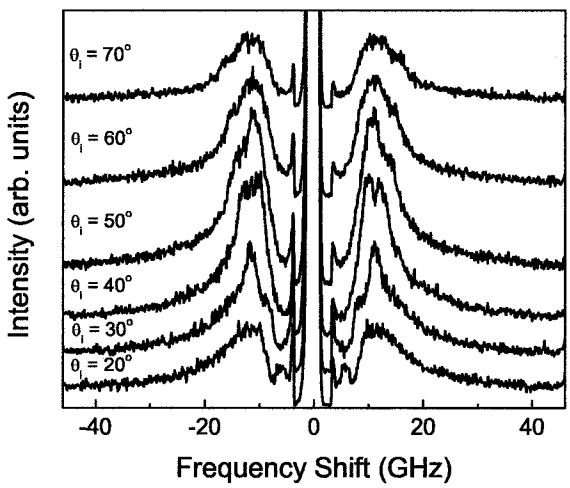

Figure 4.1: Brillouin spectra of BQ0423-15#3 (aluminum coated) for angles of incidence ranging from 20° to 70° .

are two peaks in Figure 4.1 that have frequency shifts which increase with increasing angle of incidence and three peaks that have frequency shifts which are mostly insensitive to changes in the angle of incidence. Using the analysis software to fit the peaks to a Lorentzian function, the frequency shift values were determined and are summarized in Table 4.1.

Table 4.1: Angular dependence of the frequency shifts for BQ0423-15#3 (aluminum coated).

θ_i	Frequency Shift ($\pm$0.2 GHz)				
($\pm 2^o$)	Peak 1	Peak 2	Peak 3	Peak 4	Peak 5
30	8.3	11.3	–	15.4	24.1
40	9.8	12.5	–	16.3	24.2
50	10.5	14.0	–	–	23.6
60	11.5	14.3	9.3	–	27.8
70	12.5	15.8	9.7	–	25.7

Figure 4.2 is a graph of frequency shift *versus* $\sin\theta_i$. Both peaks exhibit a linear relationship between the frequency shifts and $\sin\theta_i$. Applying a linear fit to both sets of data provides the equations $f = 9.15\sin\theta_i + 3.70$ for the first peak and $f = 9.61\sin\theta_i + 6.44$ for the second peak. The f-intercept of both fits is non-zero. This means that the peaks do not satisfy Equation (2.12) and therefore neither peak can be associated with a Rayleigh surface mode. The other three peaks have frequency shifts that are mostly insensitive to changes in angle of incidence, therefore implying that these peaks are due to bulk modes. The average shift values for each of these peaks are 9.5 GHz, 15.9 GHz, and 25.1 GHz. It should be noted that some of the bulk

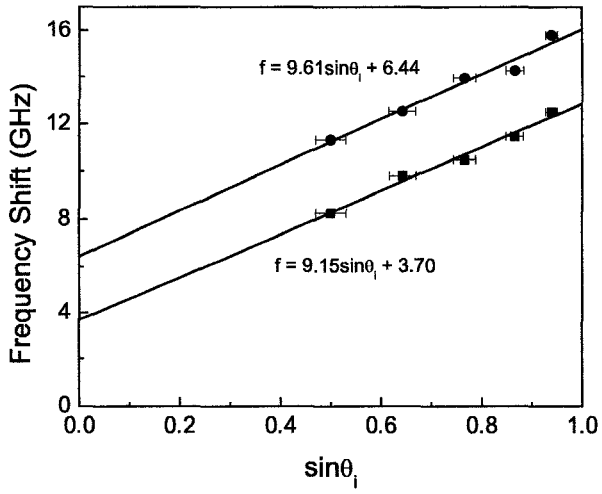

Figure 4.2: Frequency shift *versus* $\sin\theta_i$ for BQ0423-15#3 (aluminum coated).

peaks that are found in Figure 4.1 and subsequent spectra are broad and therefore are not apparent in the spectra but were discovered during peak fitting.

4.1.2 BQ0423-15#4 ($\sim$ 56% Porosity)

Figure 4.3 shows Brillouin spectra collected from BQ0423-15#4 (aluminum coated) at angles of incidence ranging from 20° to 70° at 10° intervals. These spectra were taken with a beam power of approximately 40 mW and an FSR of 50 GHz. It was found that there are two peaks in Figure 4.3 that have frequency shifts which increase with increasing angle of incidence and three peaks that have frequency shifts which are mostly insensitive to changes in the angle of incidence. The frequency shift values

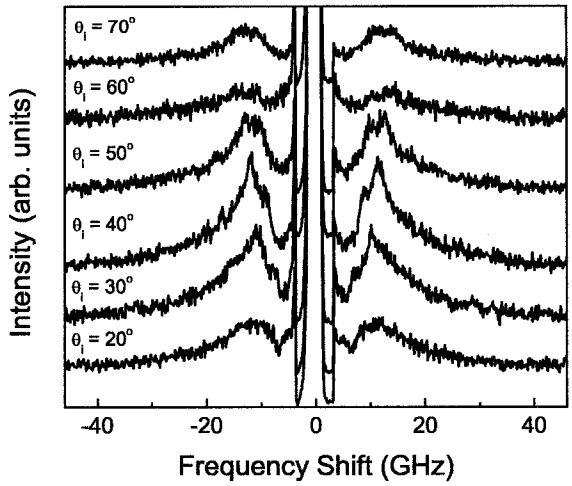

Figure 4.3: Brillouin spectra of BQ0423-15#4 (aluminum coated) for angles of incidence ranging from 20° to 70° .

were determined and are summarized in Table 4.2.

Table 4.2: Angular dependence of the frequency shifts for BQ0423-15#4 (aluminum coated).

θ_i	Frequency Shift (±0.2 GHz)				
(±2°)	Peak 1	Peak 2	Peak 3	Peak 4	Peak 5
30	7.3	10.4	13.3	18.3	–
40	8.9	11.6	14.9	–	25.3
50	9.9	12.7	15.7	–	–
60	10.4	13.8	–	19.8	30.3
70	10.8	14.2	–	18.9	25.3

Figure 4.4 is a graph of frequency shift *versus* $\sin\theta_i$. Both peaks exhibit a linear relationship between the frequency shifts and $\sin\theta_i$. Applying a linear fit provides the equations $f = 7.86\sin\theta_i + 3.61$ for the first peak and $f = 8.87\sin\theta_i + 5.95$ for

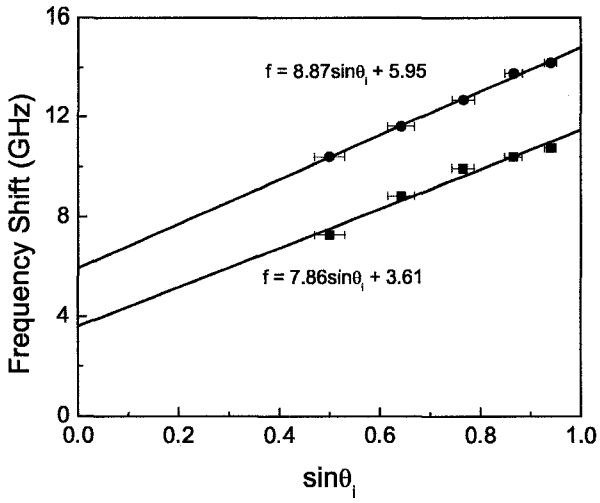

Figure 4.4: Frequency shift *versus* $\sin\theta_i$ for BQ0423-15#4 (aluminum coated).

the second peak. These two peaks can not be due to a Rayleigh surface mode while the remaining three peaks appear to be due to bulk modes. The average shift values for these peaks are 14.6 GHz, 19.0 GHz, and 27.0 GHz. The peaks with average shift positions of 15.9 GHz and 25.1 GHz are broad and therefore are not apparent in the spectra but are found during peak fitting.

4.1.3 BQ0423-15#5 ($\sim$ 58% Porosity)

BQ0423-15#5 (aluminum coated) was studied while in a near vacuum environment. Figure 4.5 shows Brillouin spectra collected from BQ0423-15#5 (aluminum coated) at angles of incidence ranging from 30° to 60° at 10° intervals. These spectra

were taken with a beam power of approximately 40 mW and an FSR of 20 GHz. It should be noted that the evenly spaced peaks located at frequency shifts less than

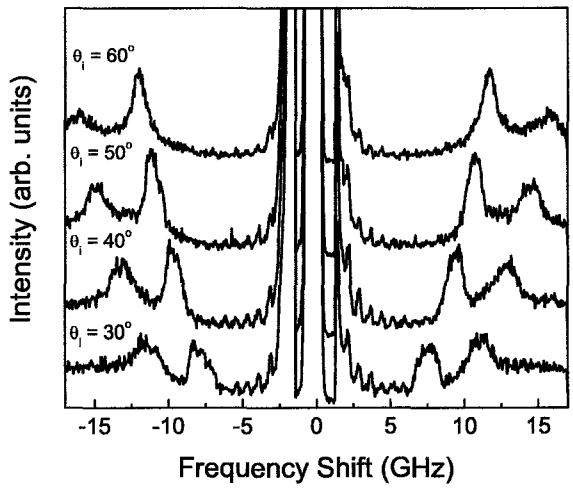

Figure 4.5: Brillouin spectra of BQ0423-15#5 (aluminum coated), while in a near vacuum environment, for angles of incidence ranging from 30° to 60° .

about 5 GHz are inherent in the experimental setup and are believed to be caused by the laser. An analysis of Figure 4.5 determined that there are two peaks that have frequency shifts which increase with increasing angle of incidence and one peak that has a frequency shift which is mostly insensitive to changes in the angle of incidence. The frequency shift values were determined and are summarized in Table 4.3. Figure 4.6 is a graph of frequency shift *versus* $\sin\theta_i$. Both peaks exhibit a linear relationship between the frequency shifts and $\sin\theta_i$. Using the method of least squares the equations $f = 11.24\sin\theta_i + 2.19$ for the first peak and $f = 12.99\sin\theta_i + 4.75$ for the second peak were determined. These two peaks cannot be due to a Rayleigh surface

Table 4.3: Angular dependence of the frequency shifts for BQ0423-15#5 (aluminum coated).

θ_i	Frequency Shift ($\pm$0.2 GHz)		
($\pm 2^o$)	Peak 1	Peak 2	Peak 3
30	7.7	11.3	15.2
40	9.5	13.0	16.1
50	10.9	14.7	14.4
60	11.8	16.0	13.8

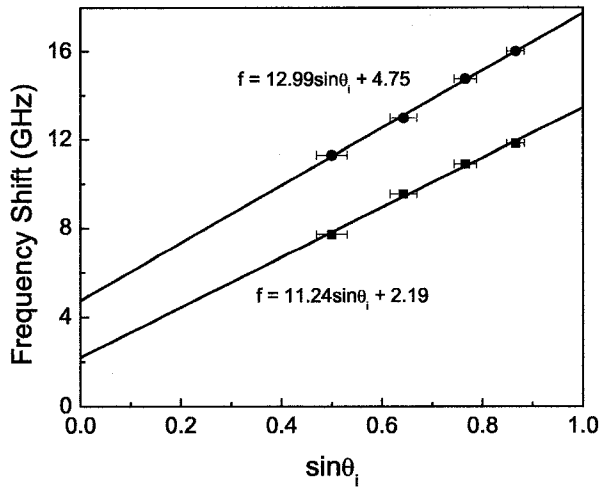

Figure 4.6: Frequency shift *versus* $\sin\theta_i$ for BQ0423-15#5 (aluminum coated).

mode while the remaining peak appears to be due to a bulk mode. The average shift value for this peak was 14.9 GHz.

4.1.4 BQ0423-15#6 ($\sim$ 30% Porosity)

Figure 4.7 shows Brillouin spectra collected from BQ0423-15#6 (aluminum coated) at angles of incidence ranging from 20° to 70° at 10° intervals. These spectra were taken with a beam power of approximately 50 mW and an FSR of 50 GHz.

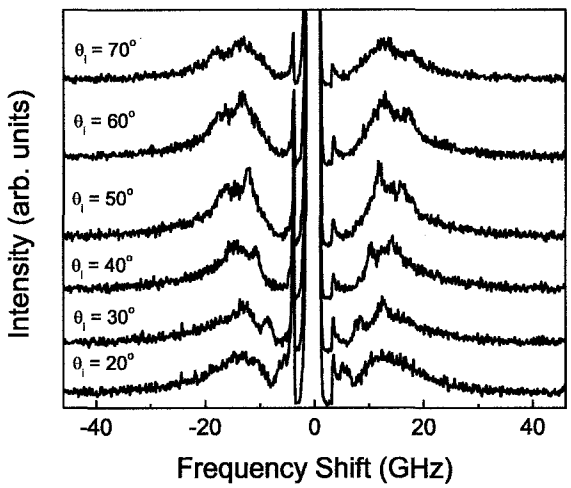

Figure 4.7: Brillouin spectra of BQ0423-15#6 (aluminum coated) for angles of incidence ranging from 20° to 70° .

Analysis software was used to determined that there are two peaks in Figure 4.7 that have frequency shifts which increase with increasing angle of incidence and three peaks that have frequency shifts which are mostly insensitive to changes in the angle of incidence. The frequency shift values were determined and are summarized in Table 4.4.

Table 4.4: Angular dependence of the frequency shifts for BQ0423-15#6 (aluminum coated).

θ_i	Frequency Shift ($\pm$0.2 GHz)				
($\pm 2^o$)	Peak 1	Peak 2	Peak 3	Peak 4	Peak 5
30	8.4	12.6	16.5	21.9	–
40	10.6	14.1	–	19.9	27.9
50	11.9	16.1	–	–	24.5
60	12.7	17.4	–	–	23.8
70	12.8	18.0	–	20.7	–

Figure 4.8 is a graph of frequency shift *versus* $\sin\theta_i$. Both peaks exhibit a linear relationship between the frequency shifts and $\sin\theta_i$. Data analysis provides the equations $f = 10.13\sin\theta_i + 3.75$ for the first peak and $f = 12.80\sin\theta_i + 6.13$ for the second peak. These two peaks can not be due to a Rayleigh surface mode while the three remaining peaks appear to be due to bulk modes. The average shift values for each of these peaks are 16.5 GHz, 20.8 GHz, and 25.4 GHz.

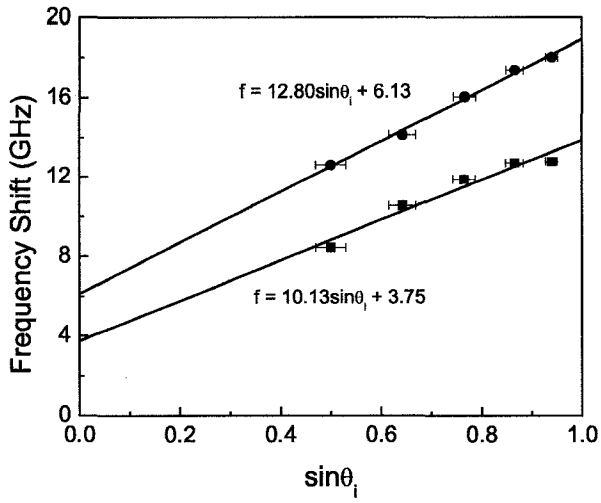

Figure 4.8: Frequency shift *versus* $\sin\theta_i$ for BQ0423-15#6 (aluminum coated).

4.1.5 BQ0423-15#9 ($\sim$ 35% Porosity)

Figure 4.9 shows Brillouin spectra collected from BQ0423-15#9 (aluminum coated) at angles of incidence ranging from 20° to 70° at 10° intervals. These spectra were taken with a beam power of approximately 50 mW and an FSR of 50 GHz. Using analysis software it was determined that there are two peaks in Figure 4.9 that have frequency shifts which increase with increasing angle of incidence and three peaks that have frequency shifts which are mostly insensitive to changes in the angle of incidence. The frequency shift values were determined and are summarized in Table 4.5. Figure 4.10 is a graph of frequency shift *versus* $\sin\theta_i$.

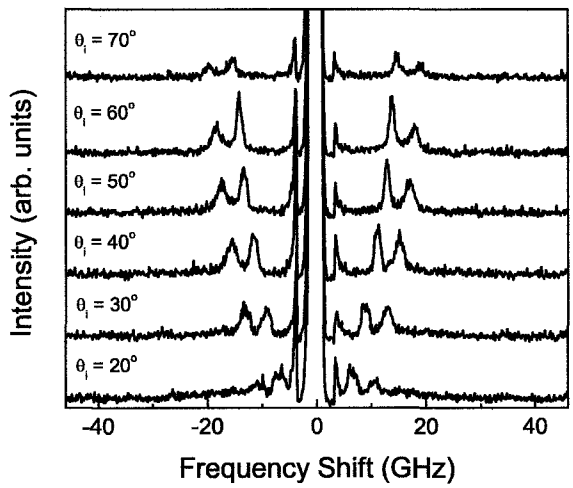

Figure 4.9: Brillouin spectra of BQ0423-15#9 (aluminum coated) for angles of incidence ranging from 20° to 70° .

Table 4.5: Angular dependence of the frequency shifts for BQ0423-15#9 (aluminum coated).

θ_i	Frequency Shift (±0.2 GHz)				
(±2°)	Peak 1	Peak 2	Peak 3	Peak 4	Peak 5
20	6.5	10.7	15.8	22.1	–
30	9.0	13.1	18.8	–	–
40	11.4	15.4	–	24.5	–
50	13.1	17.2	–	–	–
60	14.0	18.1	–	–	29.7
70	15.0	19.3	–	–	–

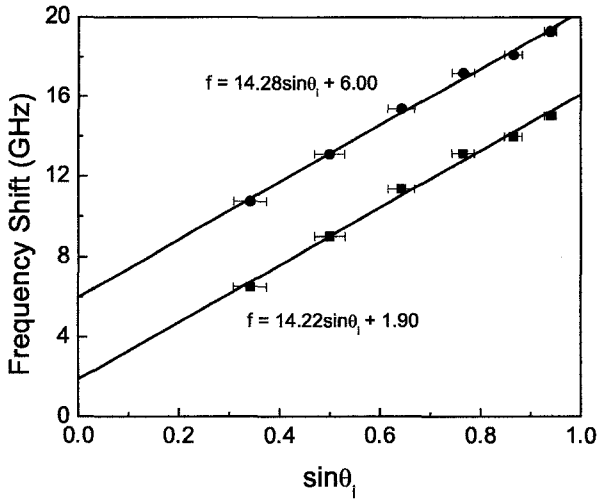

Figure 4.10: Frequency shift *versus* $\sin\theta_i$ for BQ0423-15#9 (aluminum coated).

Both peaks exhibit a linear relationship between the frequency shifts and $\sin\theta_i$. Applying a linear fit to both sets of data provides the equations $f = 14.22\sin\theta_i + 1.90$ for the first peak and $f = 14.28\sin\theta_i + 6.00$ for the second peak. These two peaks cannot be due to a Rayleigh surface mode while the three remaining peaks appear to be due to bulk modes. The average shift values for each of these peaks are 17.3 GHz, 23.3 GHz, and 29.7 GHz.

4.1.6 BQ0423-15#10 (~ 57% Porosity)

BQ0423-15#10 (aluminum coated) was studied while in a near vacuum environment. Figure 4.11 shows two spectra of BQ0423-15#10 at an angle of incidence

of 60°, one in air at atmospheric pressure and one in a near vacuum environment. These spectra were taken with a beam power of approximately 50 mW and an FSR of 50 GHz. As can be seen from Figure 4.11, the spectra are qualitatively the same.

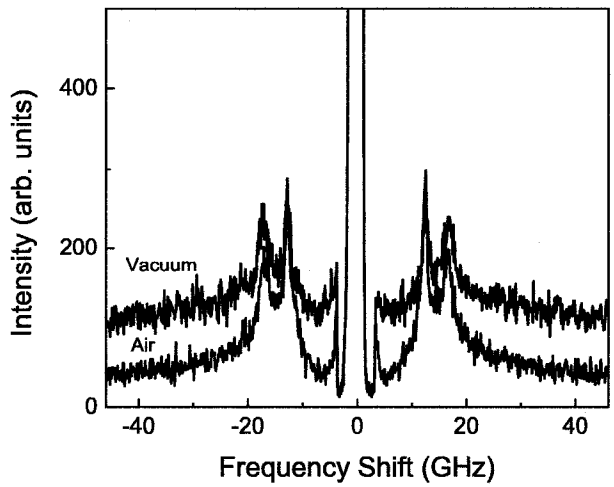

Figure 4.11: Two spectra of BQ0423-15#10 at an angle of incidence of 60°, one in air at atmospheric pressure and one in a near vacuum environment.

The only difference between the spectra is that the background level is higher for the spectrum taken with the sample in near vacuum conditions. This difference could be due to the light having to pass through a glass slide and a small slit when the sample is exposed to a near vacuum environment. This possibly reduces the size of the collection cone thereby causing the difference in the background levels. It should be noted that BQ0423-15#10 was the first sample studied and when it was determined that there is no significant difference between spectra taken in air and near vacuum it was decided to collect the remaining spectra in air.

Figure 4.12 shows Brillouin spectra collected from BQ0423-15#10 (aluminum coated) at angles of incidence ranging from 20° to 70° at 10° intervals. These spectra were taken with a beam power of approximately 50 mW and an FSR of 50 GHz. It

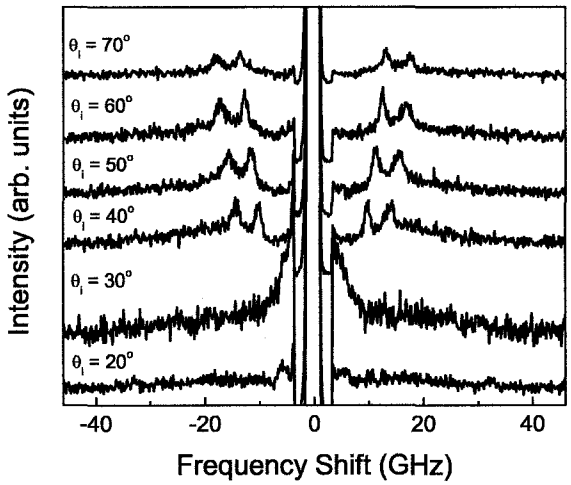

Figure 4.12: Brillouin spectra of BQ0423-15#10 (aluminum coated), while in a near vacuum environment, for angles of incidence ranging from 20° to 70° .

can be seen that the spectra for angles of incidence of 20° and 30° are significantly different than the other spectra. This could be due to a decrease in the scattering cross section that usually occurs in this range of θ_i or the sample may have been probed at a slightly different location. It was found in Figure 4.12 that there are two peaks that have frequency shifts which increase with increasing angle of incidence and one peak that has a frequency shift which is mostly insensitive to changes in the angle of incidence. The frequency shift values were determined and are summarized in Table 4.6. Figure 4.13 is a graph of frequency shift *versus* $\sin\theta_i$. Both peaks exhibit a linear

Table 4.6: Angular dependence of the frequency shifts for BQ0423-15#10 (aluminum coated).

θ_i	Frequency Shift ($\pm$0.2 GHz)		
($\pm 2^o$)	Peak 1	Peak 2	Peak 3
40	10.0	14.1	19.7
50	11.4	15.6	22.4
60	12.6	16.9	19.9
70	13.4	17.7	20.6

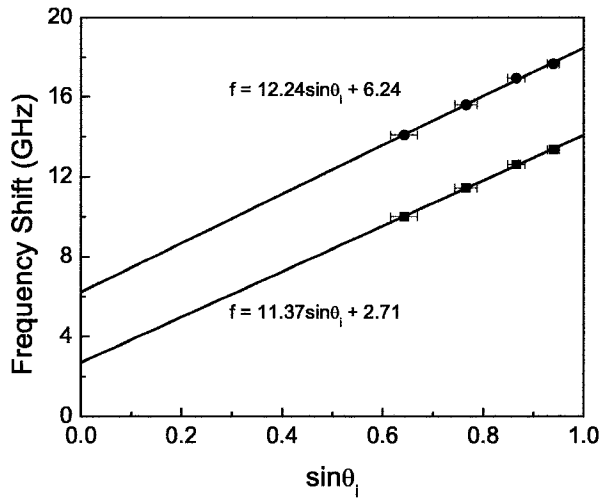

Figure 4.13: Frequency shift *versus* $\sin\theta_i$ for BQ0423-15#10 (aluminum coated).

relationship between the frequency shifts and $\sin\theta_i$. Applying a linear fit provides the equations $f = 11.37\sin\theta_i + 2.71$ for the first peak and $f = 12.24\sin\theta_i + 6.24$ for the second peak. These two peaks cannot be due to a Rayleigh surface mode while the remaining peak appears to be due to a bulk mode. The average shift value for this peak was 20.7 GHz.

4.2 Uncoated Samples

After Brillouin spectra were completed on the aluminum coated samples, each sample was subjected to acid etches in 50% HCl to remove the aluminum in an attempt to detect the surface modes and to better define the bulk modes of the PSC layers. HCl was used to remove the aluminum because, as reported in [34], it will not etch the SiC that is below the aluminum, therefore the sample should be undamaged.

4.2.1 BQ0423-15#3 ($\sim$ 39% Porosity)

Figure 4.14 shows three spectra of BQ0423-15#3 at an angle of incidence of 50°, one where the sample is aluminum coated, one after the sample had been etched for 5 minutes, and one where the sample had been etched for an additional 5 minutes. These spectra were taken with a beam power of approximately 50 mW and an FSR of 50 GHz. As can be seen in Figure 4.14, the longer the etch, the less intense the spectra collected. This is possibly due to the reflectivity of the aluminum; as more aluminum is etched the less intense the light scattering, and therefore the less intense

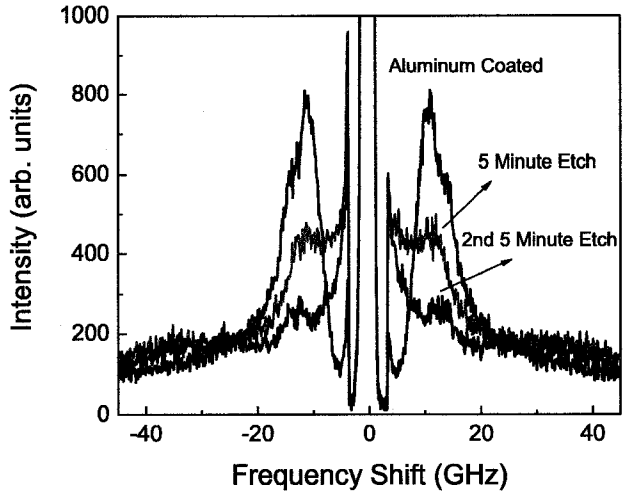

Figure 4.14: Brillouin spectra of BQ0423-15#3 for different etch conditions at an angle of incidence of 50° .

the Brillouin peaks. It was observed that after a five minute etch not all of the aluminum was removed. This seems to be confirmed in Figure 4.14 by the fact that the peaks are more intense in the five minute etch spectra than in the ten minute etch spectra. It appeared that with the ten minute etch all of the aluminum was removed which seems likely when looking at the spectra and, therefore, is considered the minimum amount of time required to remove the aluminum. It should also be noted that the first peak in the aluminum coated spectrum had a peak position of approximately 10.5 GHz and the first peak in the 10 minute etch spectrum had a peak position of approximately 12.4 GHz. Figure 4.15 shows a Brillouin spectrum taken from a piece of aluminum, at an angle of incidence of 50°, an FSR of approximately 50 GHz and a beam power of approximately 20 mW. The peak position of the first

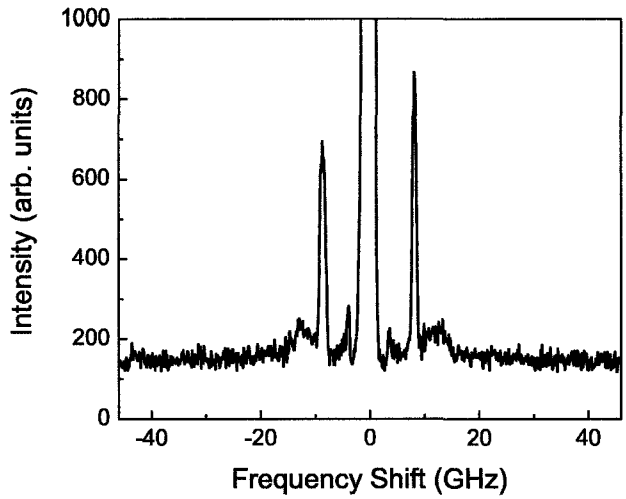

Figure 4.15: Brillouin spectra of a piece of aluminum for an angle of incidence of 50°.

peak is approximately 8.4 GHz and it is about 2 GHz lower than the peak position of the first peak in the spectrum for the aluminum coated sample. The peak position of the first peak in the aluminum coated sample is almost halfway between the peak positions for the same peak in the aluminum and 10 minute etch spectra implying that the aluminum on the aluminum coated sample provides some contribution to the spectrum.

Figure 4.16 shows Brillouin spectra collected from BQ0423-15#3 at angles of incidence ranging from 20° to 70° at 10° intervals, where the central peak is due to elastic scattering. These spectra were taken with a beam power of approximately 50 mW and an FSR of 50 GHz. An analysis of Figure 4.16 determined that there are two peaks that have frequency shifts which increase with increasing angle of incidence and

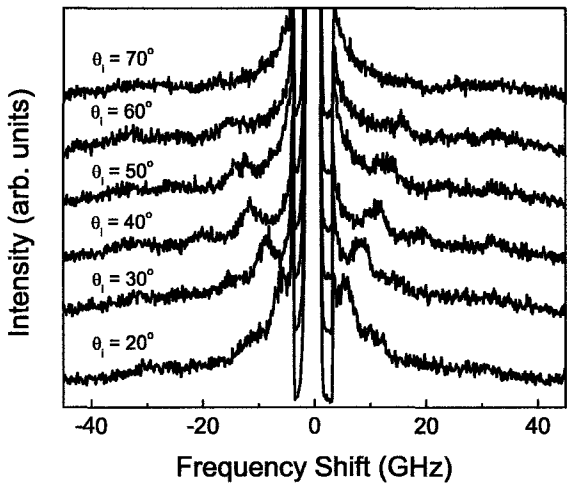

Figure 4.16: Brillouin spectra of BQ0423-15#3 for angles of incidence ranging from 20° to 70° .

two peaks that have frequency shifts which are mostly insensitive to changes in the angle of incidence. The frequency shift values were determined and are summarized in Table 4.7.

Table 4.7: Angular dependence of the frequency shifts for BQ0423-15#3 (FSR = 50 GHz).

θ_i	Frequency Shift (±0.2 GHz)			
(±2°)	Peak 1	Peak 2	Peak 3	Peak 4
20	5.5	11.1	23.9	–
30	8.0	14.9	27.0	–
40	10.7	19.9	–	31.7
50	12.4	23.9	–	33.4
60	14.0	25.2	–	33.1

Figure 4.17 is a graph of frequency shift *versus* $\sin\theta_i$ for the first two peaks. The first two peaks exhibit a linear relationship between the frequency shifts and $\sin\theta_i$. Using the method of least squares the equations $f = 16.24\sin\theta_i$ for the first peak and

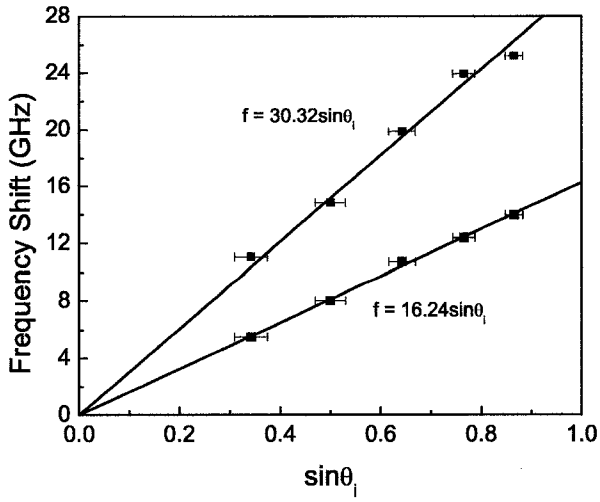

Figure 4.17: Frequency shift *versus* $\sin\theta_i$ for BQ0423-15#3.

$f = 30.32\sin\theta_i$ for the second peak were determined. The f-intercept for both fits is zero, therefore both peaks are assumed to be surface modes. The two other peaks appear to be due to bulk modes. The average shift values for each of these peaks are 25.5 GHz and 32.7 GHz.

It was suspected that the tape that was used to attach the samples to the sample holder may have contributed to the Brillouin spectra. To determine if this was the case, spectra were taken with and without the tape directly behind the sample. Figure 4.18 shows two spectra of BQ0423-15#3 at an angle of incidence of 60°, one where the

sample has tape directly behind it and one where the sample has tape at the top and bottom edges only. These spectra were taken with a beam power of approximately 50 mW and an FSR of 50 GHz. As can be seen in Figure 4.18, the only difference

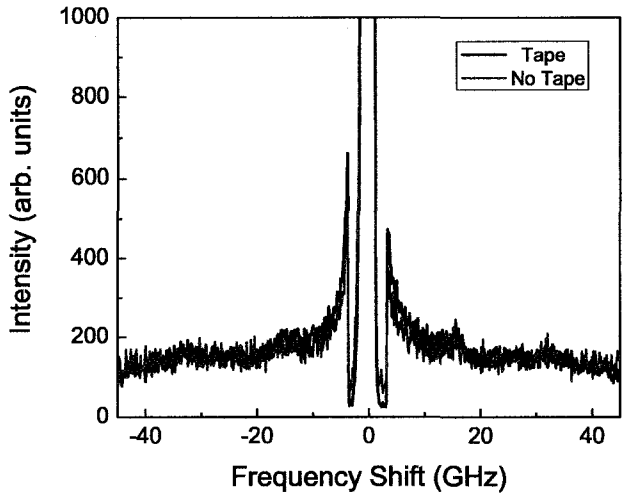

Figure 4.18: Brillouin spectra of BQ0423-15#3 for tape conditions at an angle of incidence of 60° .

between the two spectra is that when there is no tape directly behind the sample, the spectrum is noisier. Other than this the spectra are nearly identical, implying that there is no contribution to the spectra by the tape.

Spectra were then taken of BQ0423-15#3 at an FSR of approximately 106 GHz for angles of incidence of 30° and 60° . These spectra were taken with a beam power of approximately 50 mW and are shown in Figure 4.19. It should be noted that the peaks located at approximately ±106 GHz are called ghost peaks and are due to the properties of the Fabry-Perot interferometer. Six bulk peaks with frequency

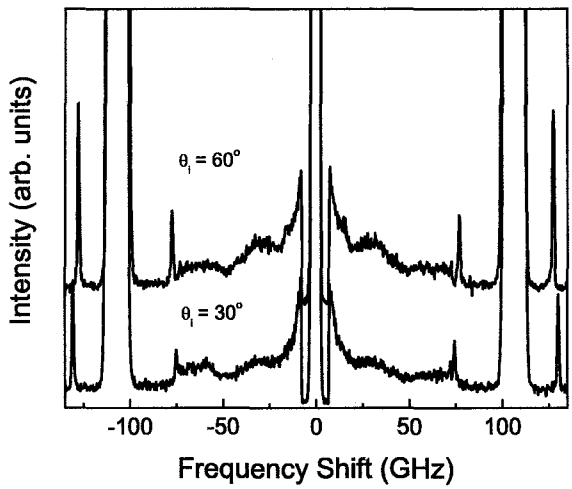

Figure 4.19: Brillouin spectra of BQ0423-15#3 for angles of incidence of 30° and 60° .

shifts greater than 40 GHz were found in Figure 4.19. The frequency shifts of these peaks are presented in Table 4.8. The average shift values for each of these peaks are 40.6 GHz, 57.5 GHz, 69.0 GHz, 72.3 GHz, 75.9 GHz, and 129.0 GHz. The peaks located at 72.3 GHz, 75.9 GHz, and 129.0 GHz are very narrow and are due to the SiC substrate [18].

Table 4.8: Angular dependence of the frequency shifts for BQ0423-15#3 (FSR = 106 GHz).

θ_i	Frequency Shift (±0.2 GHz)					
(±2°)	Peak 1	Peak 2	Peak 3	Peak 4	Peak 5	Peak 6
30	40.9	57.3	68.4	72.0	74.7	130.4
60	40.3	57.6	69.5	72.6	77.1	127.6

4.2.2 BQ0423-15#4 ($\sim$ 56% Porosity)

BQ0423-15#4 was subjected to a single 24 hour etch. It was later determined that a 10 minute etch was sufficient to remove the aluminum layers. Figure 4.20 shows Brillouin spectra collected from BQ0423-15#4 at angles of incidence ranging from 30° to 70° at 10° intervals. These spectra were taken with a beam power of approximately 40 mW and an FSR of 50 GHz. Analysis software was used to determine that there is one peak in Figure 4.20 that has a frequency shift which increases with

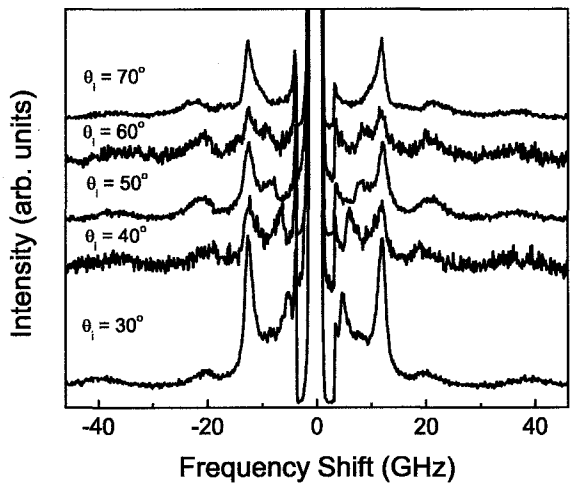

Figure 4.20: Brillouin spectra of BQ0423-15#4 for angles of incidence ranging from 30° to 70° .

increasing angle of incidence and three peaks that have frequency shifts which are mostly insensitive to changes in the angle of incidence. The frequency shift values were determined and are summarized in Table 4.9. Figure 4.21 is a graph of frequency shift *versus* $\sin\theta_i$.

Table 4.9: Angular dependence of the frequency shifts for BQ0423-15#4 (FSR = 50 GHz).

θ_i	Frequency Shift ($\pm$0.2 GHz)			
($\pm 2^o$)	Peak 1	Peak 2	Peak 3	Peak 4
30	5.0	12.1	20.4	39.3
40	6.5	11.9	19.8	36.2
50	8.3	12.3	21.2	37.1
60	8.8	12.2	20.9	35.6
70	10.6	12.2	22.1	36.9

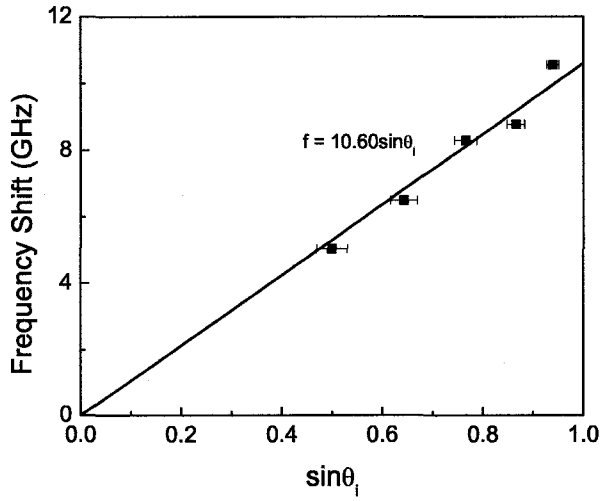

Figure 4.21: Frequency shift *versus* $\sin\theta_i$ for BQ0423-15#4.

This peak exhibits a linear relationship between the frequency shift and $\sin\theta_i$. Data analysis yields the equation $f = 10.60 \sin\theta_i$. This peak appears to be due to a surface mode while the three remaining peaks appear to be due to bulk modes. The average shift values for each of these peaks are 12.1 GHz, 20.9 GHz, and 37.0 GHz.

BQ0423-15#4 was then subjected to an additional 48 hour etch. This was intended to be a 24 hour etch but was inadvertently etched for 48 hours. Figure 4.22 shows two spectra of BQ0423-15#4, one after the 24 hour etch and one after the 72 hour etch. The spectrum for the 24 hour etch was taken for twice the length of time than for the spectrum for the 72 hour etch. The spectra were taken for a 60° angle of incidence, an FSR of 50 GHz, and a beam power of approximately 40 mW for the 24 hour etch and approximately 50 mW for the 72 hour etch. It can be seen in Figure 4.22 that the two outer peaks have greater frequency shifts for the longer etch conditions. The two peaks were found at 20.9 GHz and 35.6 GHz for the 24 hour etch spectra. After the 72 hour etch these peaks were found at 23.2 GHz and 39.0 GHz. Though some deviation would be expected, a difference in frequency shifts of approximately 2 and 3 GHz respectively is larger than expected. This implies that there is some fundamental change, such as an increase in porosity, to the structure of the sample with the longer etch. It should also be noted that the surface mode is not affected by the longer etch, but two of the three assumed bulk modes are affected. This implies that the surface of the porous layer is not affected by the additional etch time while the bulk of the porous layer is affected.

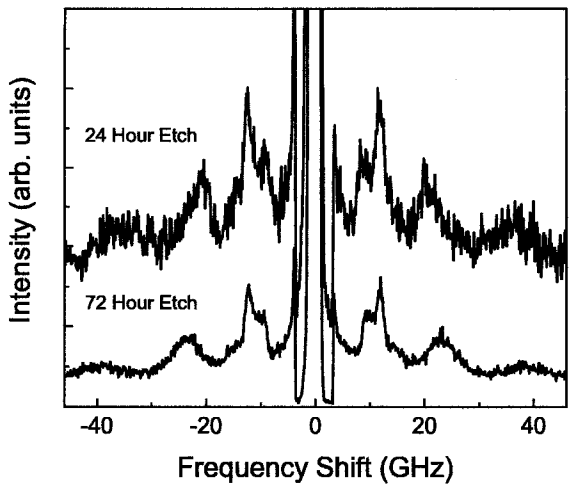

Figure 4.22: Brillouin spectra of BQ0423-15#4 at an angle of incidence of 60° after a 24 hour etch and a 72 hour etch.

BQ0423-15#4 was then placed in the drying system to try to remove any water that may have collected in the porous layer. The sample was subjected to a temperature of approximately 164°C in a near vacuum environment for $\sim$ 5 hours. The sample was then transferred from the drying system to the vacuum sample holder. Due to the equipment used, the sample had to be subjected to air during the transfer but this was for a period of time that was less than 5 minutes and should not have allowed any significant amount of moisture to build up on the sample. Figure 4.23 shows two spectra of BQ0423-15#4 at an angle of incidence of 60°, one of the sample in air and the other of the sample in near vacuum after it had been dried. The spectrum for the sample after it had been dried was collected for 25% less time than the spectrum for the sample

before it had been dried. Both spectra were taken with an FSR of 50 GHz and a beam power of approximately 50 mW. It can be seen in Figure 4.23 that there is very

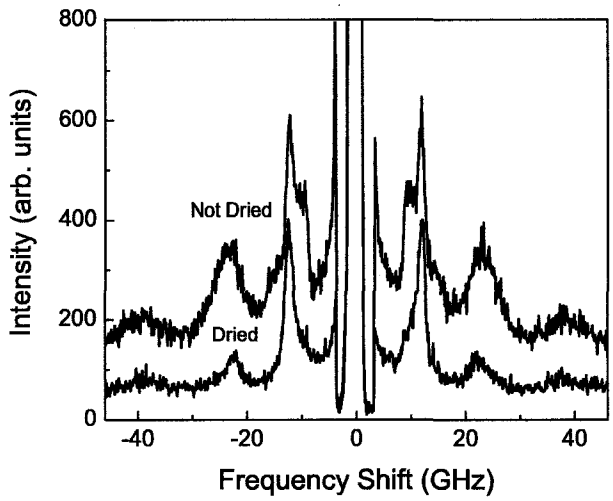

Figure 4.23: Brillouin spectra of BQ0423-15#4 at an angle of incidence of 60° before and after being dried.

little difference between the two spectra. The intensity difference between the spectra is due in part to the shorter collection time for the dried sample spectrum. The peak positions for each spectrum were almost identical but the intensity ratio of the first two peaks is smaller for the spectrum that was taken after the sample had been dried. This could imply that water in the sample had some affect on the Brillouin spectra but there is insufficient data to say for certain why there is a difference.

Spectra were then taken of BQ0423-15#4 at a FSR of approximately 106 GHz for angles of incidence of 30° and 60° . These spectra were taken with a beam power of approximately 50 mW and are shown in Figure 4.24. Four bulk peaks with frequency

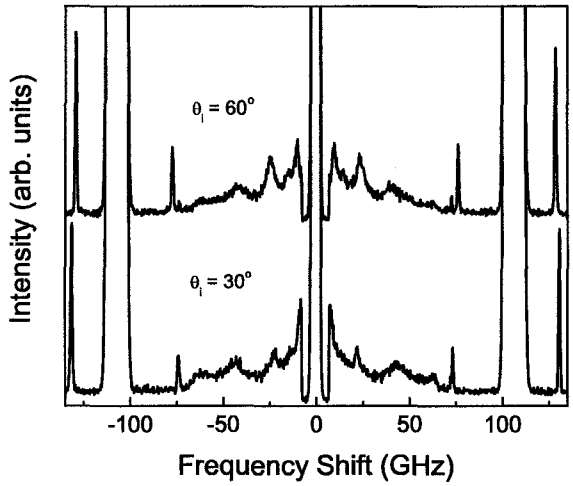

Figure 4.24: Brillouin spectra of BQ0423-15#4 for angles of incidence of 30° and 60° .

shifts greater than 40 GHz were found in Figure 4.24. The frequency shifts of these peaks are presented in Table 4.10.

Table 4.10: Angular dependence of the frequency shifts for BQ0423-15#4 (FSR = 106 GHz).

θ_i	Frequency Shift (±0.2 GHz)			
($\pm 2^o$)	Peak 1	Peak 2	Peak 3	Peak 4
30	61.8	–	73.7	131.1
60	60.8	73.0	76.7	128.9

The average shift values for each of these peaks are 61.3 GHz, 73.0 GHz, 75.2 GHz, and 130.0 GHz. The peaks located at 73.0 GHz, 75.2 GHz, and 130.0 GHz are very narrow and are due to the SiC substrate.

4.2.3 BQ0423-15#5 ($\sim$ 58% Porosity)

BQ0423-15#5 was subjected to a single one hour etch. Figure 4.25 shows Brillouin spectra collected from BQ0423-15#5 at angles of incidence ranging from 20° to 70° at 10° intervals. These spectra were taken with a beam power of approximately 50 mW and an FSR of 50 GHz. Using analysis software it was determined that there are two

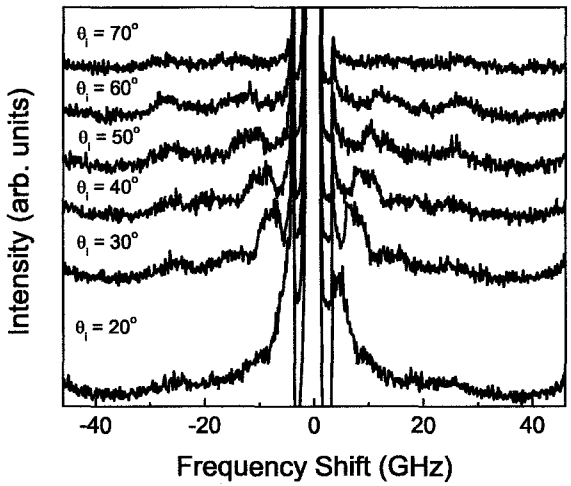

Figure 4.25: Brillouin spectra of BQ0423-15#5 for angles of incidence ranging from 20° to 70° .

peaks in Figure 4.25 that have frequency shifts which increase with increasing angle of incidence and three peaks that have frequency shifts which are mostly insensitive to changes in the angle of incidence. The frequency shift values were determined and are summarized in Table 4.11. Figure 4.26 is a graph of frequency shift *versus* $\sin\theta_i$. Both peaks exhibit a linear relationship between the frequency shifts and $\sin\theta_i$. Applying a linear fit to both sets of data gives $f = 13.21\sin\theta_i$ for the first peak and

Table 4.11: Angular dependence of the frequency shifts for BQ0423-15#5 (FSR = 50 GHz).

θ_i	Frequency Shift ($\pm$0.2 GHz)				
($\pm 2^o$)	Peak 1	Peak 2	Peak 3	Peak 4	Peak 5
20	4.3	–	10.3	20.7	22.2
30	6.6	8.7	–	14.9	25.3
40	8.2	11.1	–	17.8	25.9
50	10.1	13.5	–	19.0	25.9
60	11.6	13.5	–	–	26.8
70	12.5	17.0	–	–	27.1

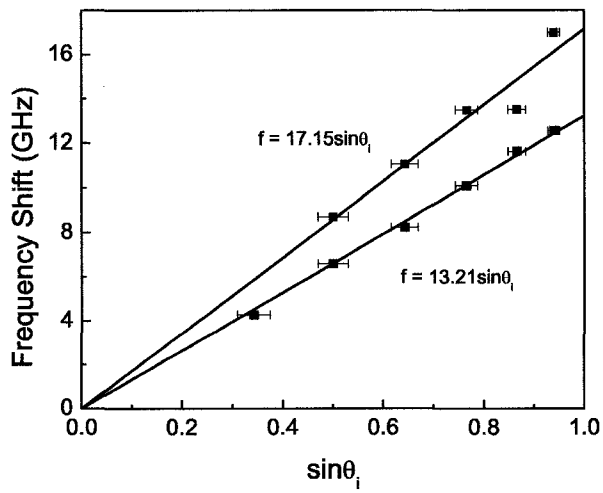

Figure 4.26: Frequency shift *versus* $\sin\theta_i$ for BQ0423-15#5.

$f = 17.15 \sin\theta_i$ for the second peak. These two peaks appear to be due to surface modes while the three remaining peaks appear to be due to bulk modes. The average shift values for each of these peaks are 10.3 GHz, 18.1 GHz, and 25.5 GHz.

Spectra were then taken of BQ0423-15#5 at a FSR of approximately 106 GHz for angles of incidence of 30° and 60° . These spectra were taken with a beam power of approximately 50 mW and are shown in Figure 4.27. Five bulk peaks with frequency

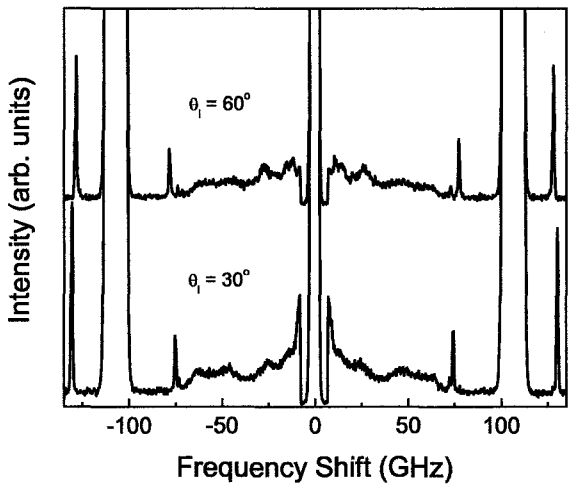

Figure 4.27: Brillouin spectra of BQ0423-15#5 for angles of incidence of 30° and 60° .

shifts greater than 30 GHz were found in Figure 4.27. The frequency shifts of these peaks are presented in Table 4.12. The average values for each of these peaks are 46.5 GHz, 61.5 GHz, 72.9 GHz, 76.2 GHz, and 129.4 GHz. The peaks located at 72.9 GHz, 76.2 GHz, and 129.4 GHz are very narrow and are due to the SiC substrate.

Table 4.12: Angular dependence of the frequency shifts for BQ0423-15#5 (FSR = 106 GHz).

θ_i	Frequency Shift (±0.2 GHz)				
(±2°)	Peak 1	Peak 2	Peak 3	Peak 4	Peak 5
30	47.1	62.6	72.6	74.6	130.5
60	45.9	60.4	73.2	77.7	128.3

4.2.4 BQ0423-15#6 (~ 30% Porosity)

BQ0423-15#6 was subjected to two separate 5 minute etches. Figure 4.28 shows Brillouin spectra collected from BQ0423-15#6 at angles of incidence ranging from 20° to 70° at 10° intervals. These spectra were taken with a beam power of approximately 50 mW and an FSR of 50 GHz. It was found that there is one peak in Figure 4.28 that has a frequency shift which increases with increasing angle of incidence and

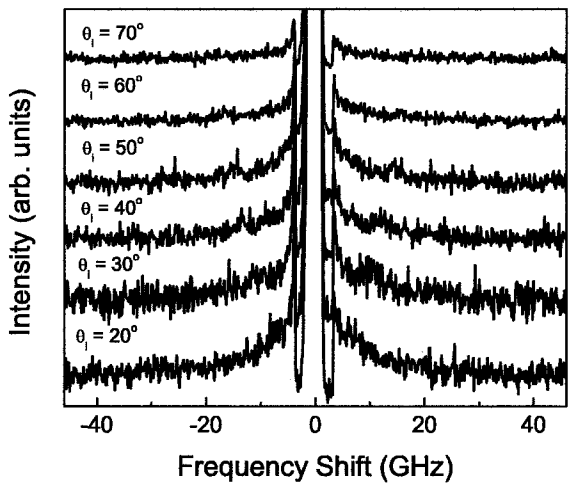

Figure 4.28: Brillouin spectra of BQ0423-15#6 for angles of incidence ranging from 20° to 70° .

three peaks that have frequency shifts which are mostly insensitive to changes in the angle of incidence. The frequency shift values were determined and are summarized in Table 4.13. Figure 4.29 is a graph of frequency shift *versus* $\sin\theta_i$.

Table 4.13: Angular dependence of the frequency shifts for BQ0423-15#6 (FSR = 50 GHz).

θ_i	Frequency Shift (±0.2 GHz)			
(±2°)	Peak 1	Peak 2	Peak 3	Peak 4
20	6.4	9.5	–	29.0
30	9.6	–	20.4	–
40	12.7	–	–	–
50	14.5	–	23.7	–
60	16.0	–	19.6	30.0
70	17.5	–	–	28.7

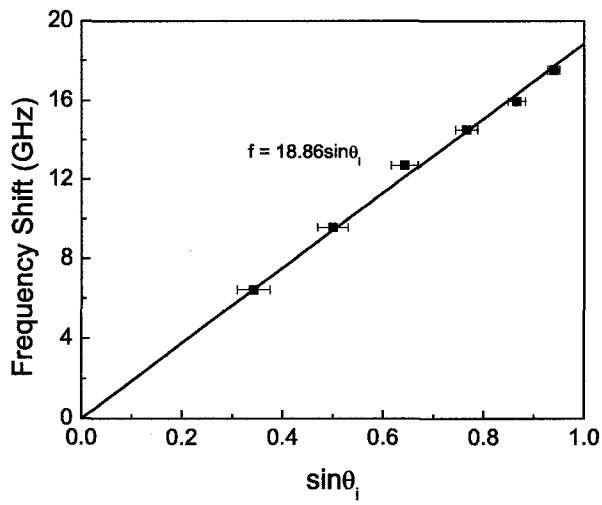

Figure 4.29: Frequency shift *versus* $\sin\theta_i$ for BQ0423-15#6.

This peak exhibits a linear relationship between the frequency shift and $\sin\theta_i$. Applying a linear fit yields the equation $f = 18.86 \sin\theta_i$. This peak appears to be due to a surface mode while the three remaining peaks appear to be due to bulk modes. The average shift values for each of these peaks are 9.5 GHz, 21.2 GHz, and 29.2 GHz.

Spectra were then taken of BQ0423-15#6 at a FSR of approximately 106 GHz for angles of incidence of 30° and 60° . These spectra were taken with a beam power of approximately 50 mW and are shown in Figure 4.30. Five bulk peaks with frequency

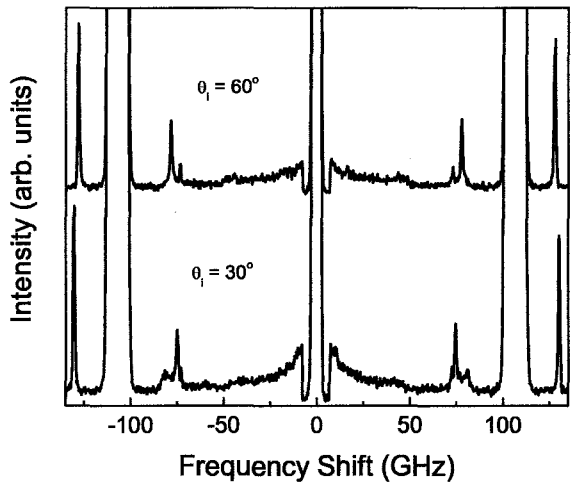

Figure 4.30: Brillouin spectra of BQ0423-15#6 for angles of incidence of 30° and 60° .

shifts greater than 30 GHz can be seen in Figure 4.30. The frequency shifts of these peaks are presented in Table 4.14. The average shift values for each of these peaks are 43.7 GHz, 72.9 GHz, 76.4 GHz, 80.3 GHz, and 129.2 GHz. The peaks located at 72.9 GHz, 76.4 GHz, and 129.2 GHz are very narrow and are due to the SiC substrate.

Table 4.14: Angular dependence of the frequency shifts for BQ0423-15#6 (FSR = 106 GHz).

θ_i	Frequency Shift (±0.2 GHz)				
(±2°)	Peak 1	Peak 2	Peak 3	Peak 4	Peak 5
30	42.0	72.6	74.7	80.3	130.3
60	45.3	73.2	78.0	–	128.0

4.2.5 BQ0423-15#9 (~ 35% Porosity)

BQ0423-15#9 was subjected to two separate 5 minute etches. Figure 4.31 shows Brillouin spectra collected from BQ0423-15#9 at angles of incidence ranging from 20° to 70° at 10° intervals. These spectra were taken with a beam power of approximately 50 mW and an FSR of 50 GHz. An analysis of Figure 4.31 determined that there are two peaks that have frequency shifts which increase with increasing angle

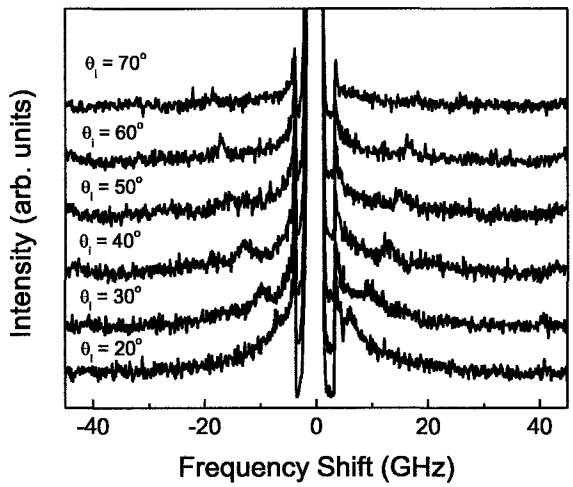

Figure 4.31: Brillouin spectra of BQ0423-15#9 for angles of incidence ranging from 20° to 70° .

of incidence and three peaks that have frequency shifts which are mostly insensitive to changes in the angle of incidence. The frequency shift values were determined and are summarized in Table 4.15.

Table 4.15: Angular dependence of the frequency shifts for BQ0423-15#9 (FSR = 50 GHz).

θ_i	Frequency Shift ($\pm$0.2 GHz)				
($\pm 2^o$)	Peak 1	Peak 2	Peak 3	Peak 4	Peak 5
20	6.2	10.3	–	18.3	–
30	9.2	16.1	–	–	24.0
40	12.5	19.7	–	–	27.2
50	15.6	25.4	10.5	–	–
60	16.7	–	–	–	–
70	18.1	29.6	–	–	–

Figure 4.32 is a graph of frequency shift *versus* $\sin\theta_i$. Both peaks exhibit a linear relationship between the frequency shifts and $\sin\theta_i$. Using the method of least squares the equations $f = 19.40\sin\theta_i$ for the first peak and $f = 31.74\sin\theta_i$ for the second peak were determined. These two peaks appear to be due to surface modes while the three remaining peaks appear to be due to bulk modes. The average shift values for each of these peaks are 10.5 GHz, 18.3 GHz, and 25.6 GHz.

Spectra were then taken of BQ0423-15#9 at a FSR of approximately 106 GHz for angles of incidence of 30° and 60° . These spectra were taken with a beam power of approximately 50 mW and are shown in Figure 4.33. Five bulk peaks with frequency shifts greater than 30 GHz were found in Figure 4.33. The frequency shifts of these peaks are presented in Table 4.16.

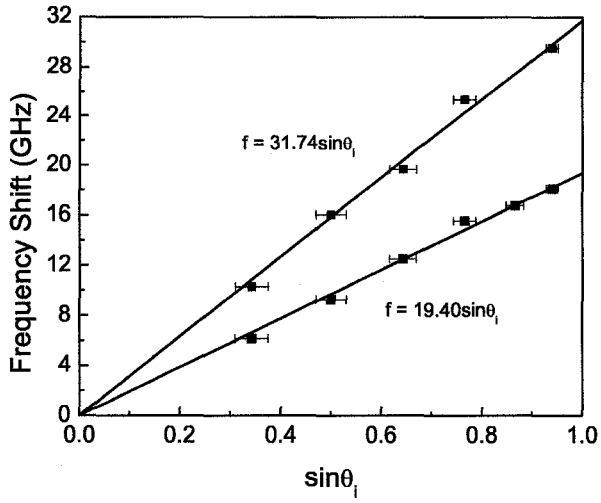

Figure 4.32: Frequency shift *versus* $\sin\theta_i$ for BQ0423-15#9.

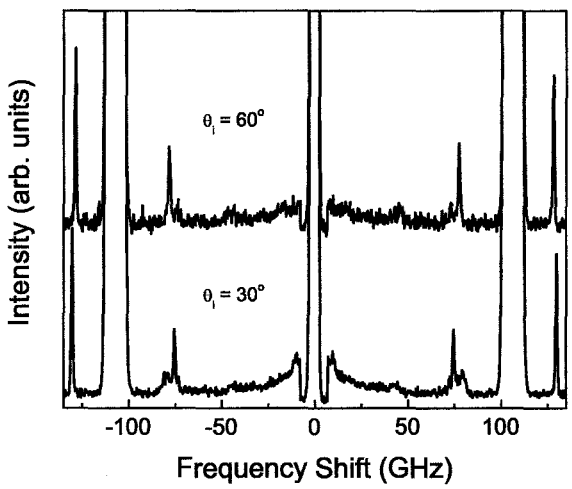

Figure 4.33: Brillouin spectra of BQ0423-15#9 for angles of incidence of 30° and 60° .

Table 4.16: Angular dependence of the frequency shifts for BQ0423-15#9 (FSR = 106 GHz).

θ_i	Frequency Shift ($\pm$0.2 GHz)				
($\pm 2^o$)	Peak 1	Peak 2	Peak 3	Peak 4	Peak 5
30	43.0	72.6	74.9	79.5	130.1
60	45.3	73.3	77.8	–	128.4

The average shift values for each of these peaks are 44.2 GHz, 73.0 GHz, 76.4 GHz, 79.5 GHz, and 129.3 GHz. The peaks located at 73.0 GHz, 76.4 GHz, and 129.3 GHz are very narrow and are due to the SiC substrate.

4.2.6 BQ0423-15#10 ($\sim$ 57% Porosity)

BQ0423-15#10 was subjected to two separate 5 minute etches. Figure 4.34 shows Brillouin spectra collected from BQ0423-15#10 at angles of incidence ranging from 20° to 70° at 10° intervals. These spectra were taken with a beam power of approximately 50 mW and an FSR of 50 GHz. Analysis software was used to determine that there are two peaks in Figure 4.34 that have frequency shifts which increase with increasing angle of incidence and two peaks that have frequency shifts which are mostly insensitive to changes in the angle of incidence. The frequency shift values were determined and are summarized in Table 4.17. Figure 4.35 is a graph of frequency shift *versus* $\sin\theta_i$. Both peaks exhibit a linear relationship between the frequency shifts and $\sin\theta_i$. Data analysis gives the equations $f = 16.73\sin\theta_i$ for the first peak and $f = 29.07\sin\theta_i$ for the second peak. These two peaks appear to be due to surface

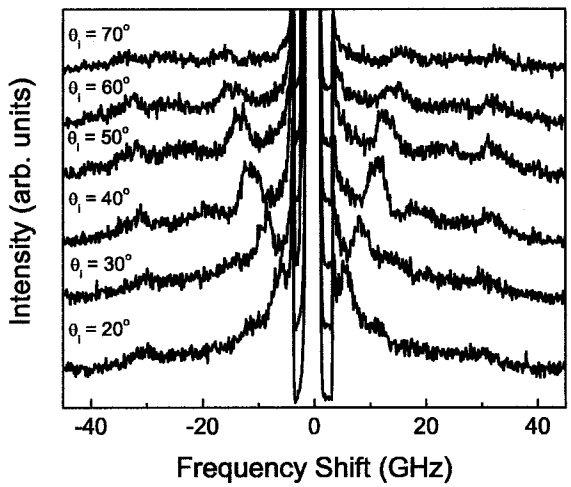

Figure 4.34: Brillouin spectra of BQ0423-15#10 for angles of incidence ranging from 20° to 70° .

Table 4.17: Angular dependence of the frequency shifts for BQ0423-15#10 (FSR = 50 GHz).

θ_i	Frequency Shift (±0.2 GHz)			
($\pm 2^o$)	Peak 1	Peak 2	Peak 3	Peak 4
20	5.7	11.3	19.1	30.5
30	8.3	12.8	–	29.7
40	11.1	19.6	–	31.0
50	12.9	23.2	–	32.1
60	14.1	25.3	–	32.6
70	15.9	26.3	–	33.5

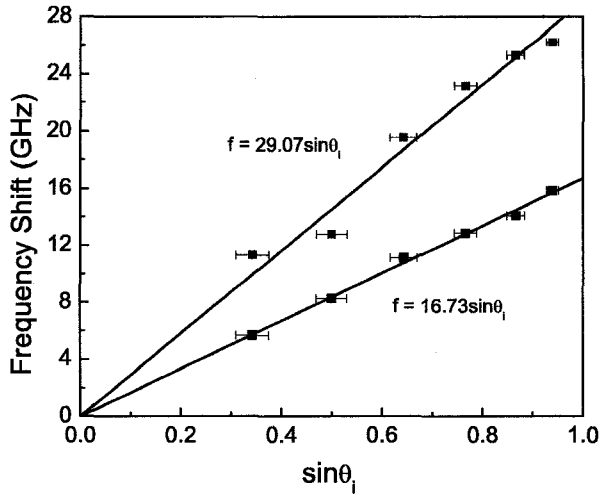

Figure 4.35: Frequency shift *versus* $\sin\theta_i$ for BQ0423-15#10.

modes while the two remaining peaks appear to be due to bulk modes. The average shift values for each of these peaks are 19.1 GHz and 31.6 GHz.

Spectra were then taken of BQ0423-15#10 at a FSR of approximately 106 GHz for angles of incidence of 30° and 60° . These spectra were taken with a beam power of approximately 50 mW and are shown in Figure 4.36. Five bulk peaks with frequency shifts greater than 35 GHz can be seen in Figure 4.36. The frequency shifts of these peaks are presented in Table 4.18. The average shift values for each of these peaks are 58.0 GHz, 67.3 GHz, 72.5 GHz, 75.2 GHz, and 130.2 GHz. The peaks located at 72.5 GHz, 75.2 GHz, and 130.2 GHz are very narrow and are due to the SiC substrate.

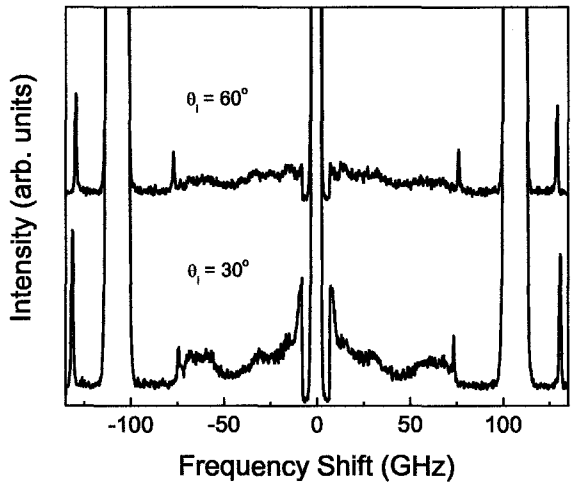

Figure 4.36: Brillouin spectra of BQ0423-15#10 for angles of incidence of 30° and 60° .

Table 4.18: Angular dependence of the frequency shifts for BQ0423-15#10 (FSR = 106 GHz).

θ_i	Frequency Shift (±0.2 GHz)				
($\pm 2^o$)	Peak 1	Peak 2	Peak 3	Peak 4	Peak 5
30	58.9	68.3	72.1	73.9	131.0
60	57.1	66.3	72.8	76.5	129.3

4.3 Discussion

4.3.1 Aluminum Coated Samples

It was initially expected that the spectra for the aluminum coated samples would show a Rayleigh surface mode and potentially some bulk modes as well. It has been found that there are in fact no Rayleigh surface modes present. That said, there are two modes in each sample which have frequency shifts which increase linearly with $\sin\theta_i$ but that have a non-zero f-intercept. Rayleigh surface modes display the same linear relationship between frequency shift and $\sin\theta_i$ but the f-intercept is zero, as can be seen in Equation (2.12). There is a chance that the linear relationship which the two peaks exhibit could mean they have a relationship to Rayleigh surface modes, but there is insufficient evidence to classify these peaks. There were also a number of weak bulk modes found from the spectra for the aluminum coated samples. These peaks were ignored because the bulk peaks were found in the spectra taken after the aluminum had been removed.

4.3.2 Uncoated Samples

Surface Modes

Using Equation (2.12), the surface velocities can be determined for each sample and are summarized in Table 4.19.

Table 4.19: Surface Wave Velocities

Sample Name	Porosity (%)	Surface Wave Velocity ($\times 10^3$ m/s)	
		Peak 1	Peak 2
BQ0423-15#3	39 ± 8	4.3 ± 0.2	8.1 ± 0.3
BQ0423-15#4	56 ± 11	2.8 ± 0.1	–
BQ0423-15#5	58 ± 12	3.5 ± 0.1	4.6 ± 0.2
BQ0423-15#6	30 ± 6	5.0 ± 0.2	–
BQ0423-15#9	35 ± 7	5.2 ± 0.2	8.4 ± 0.3
BQ0423-15#10	57 ± 11	4.5 ± 0.2	7.7 ± 0.3

There can only be one Rayleigh surface mode found for a sample, therefore one of these modes would be the Rayleigh surface mode whereas the other peak could be due to a pseudo-surface mode. Pseudo-surface modes are essentially surface modes that radiate a small amount of energy into the bulk of the sample, thereby attenuating particle displacements in the direction of propagation [35].

Devaty and coworkers at the University of Pittsburgh provided a theoretical model that calculated acoustic wave velocities as a function of porosity. This model is known as the Mori-Tanaka acoustic effective medium model and is based on work done by T. Mori and K. Tanaka [36]. Of particular importance to the model is the shape of the pores of the material. The shape factor is represented by ξ and is equal to $\frac{a}{c}$. a and c were determined by assuming the pores were ellipsoids, where a is the axis perpendicular to the c-axis and c is the axis parallel to the c-axis [37]. Figure 4.37 is a graph that shows the Rayleigh surface wave velocities as a function of porosity for 6H-SiC with three different ξ values and was provided by Dr. Devaty and coworkers. The values of ξ that were used were 0.2, 1, and 5, which represent prolate spheroid,

spherical, and oblate spheroid pore shapes respectively. The Rayleigh surface wave velocities that were experimentally determined for the first peak (see Table 4.19) are also presented in Figure 4.37. It can be seen in Figure 4.37 that the velocities from

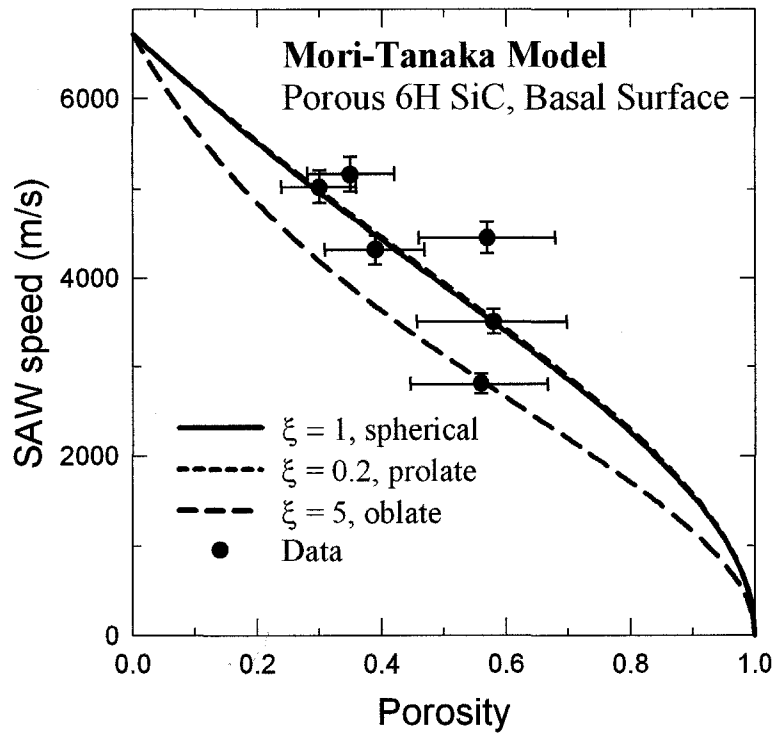

Figure 4.37: Mori Tanaka model of Rayleigh surface wave velocities for spherical, prolate spheroid and oblate spheroid pore shapes.

the first peak agree fairly well with the Mori-Tanaka model for both spherical and prolate spheroid shaped pores which, together with the good fit of Equation (2.12) to the Brillouin data, indicates that the first peak is assuredly due to the Rayleigh surface mode. Three of the data points fall almost exactly on the curves that represent both

spherical and prolate spheroid pore shapes. Two others are located somewhat above these curves but are in reasonable agreement with them. This could be explained by the fact that there is a large uncertainty in the porosities of the samples, therefore the two samples could have porosities different from what is reported. The results thus imply that the pore shape for the PSC samples can be modeled as either spheres or prolate spheroids. It should be noted, however, that branched morphology PSC looks very much like a coral reef with pores of varying shapes and sizes and does not have one single pore shape. It is possible that future work on the model could allow for an estimate of the distribution of pore shapes to be determined.

The final data point happens to lie on the curve that represents an oblate spheroid pore shape. This was unexpected because all of the samples were fabricated by the same method and it would be expected that the creation of pores, and therefore the pore shape, should then be the same for each sample. This anomaly, however, may be able to be explained by the fact that this particular data point is from sample, BQ0423-15#4, which was subjected to the longest HCl etch to remove its aluminum coating. If HCl happens to etch SiC to even some small degree, there could be a considerable change in the porosity. As can be seen in Figure 4.37 the higher the porosity the lower the velocity, therefore, if there was an increase in porosity it would indicate why the Rayleigh surface wave velocity for BQ0423-15#4 is lower than expected. It is of particular interest to note that based on the Rayleigh surface wave velocity and the Mori-Tanaka model that the porosity of BQ0423-15#4 is approximately 70%.

The second peak in Table 4.19 could be due to a pseudo-surface mode. According to [38], pseudo-surface modes have frequency shifts that can exhibit the same relationship with $\sin\theta_i$ as Rayleigh surface modes. Pseudo-surface modes also have velocities that are higher than those of Rayleigh surface modes. The velocity of a pseudo-surface mode can be higher than the second transverse bulk wave velocity but must still be lower than the longitudinal bulk wave velocity [39]. Additional experimentation is required to confirm that the observed mode is in fact a pseudo-surface mode.

Bulk Modes

To determine the bulk mode velocities for each sample, it is necessary to have the refractive index of each sample. SiC is a birefringent material and as such has two refractive index values, the ordinary refractive index, n_o, and the extraordinary refractive index, n_e. According to [40],

$$n_o = 2.5531 + \frac{0.0334 \times 10^6}{\lambda^2} \tag{4.1}$$

and

$$n_e = 2.5852 + \frac{0.0368 \times 10^6}{\lambda^2} \tag{4.2}$$

for 6H SiC. For a wavelength of 532 nm it is found that $n_o = 2.671$ and $n_e = 2.715$. The ordinary and extraordinary refractive index values of the porous material can be determined using the Maxwell-Garnett effective dielectric approximation as outlined by Devaty and Sievers [41]. Taking the equation outlined in [41], using the fact that

the dielectric function is equal to the refractive index squared, and assuming that the pores are filled with air, allows an equation for the effective refractive index of the porous layer, $\overline{n}$, to be determined such that,

$$\overline{n} = \sqrt{\frac{(1-L)n^2 - p(1-L)n^2 - p(L-1) + L}{L(1-p) + n^2(1-L+pL)}}, \tag{4.3}$$

where n is the refractive index of the material that the porous layer was etched from, p is the porosity of the porous layer, and L is the depolarization factor. If $\frac{n_e a}{n_o c} < 1$, the depolarization factor that relates to the extraordinary refractive index is

$$L_{\parallel} = \frac{1-e^2}{2e^3}\left(\ln\left|\frac{1+e}{1-e}\right| - 2e\right), \tag{4.4}$$

and if $\frac{n_e a}{n_o c} > 1$ the depolarization factor that relates to the extraordinary refractive index is

$$L_{\parallel} = \frac{1+e^2}{e^3}(e - \tan^{-1} e). \tag{4.5}$$

The depolarization factor that relates to the ordinary refractive index is then

$$L_{\perp} = \frac{1-L_{\parallel}}{2}, \tag{4.6}$$

where

$$e = \left|\left(\frac{n_e a}{n_o c}\right)^2 - 1\right|^{\frac{1}{2}}. \tag{4.7}$$

Based on the results from Figure 4.37, it is known that the pore shapes for the PSC samples can be successfully modeled as either spheres or prolate spheroids. Using Equation (4.3), the ordinary and extraordinary refractive index values for SiC, the shape factor of 1 for spherical pore shapes, and the appropriate depolarization

factors, the effective refractive index values for each sample were determined, along with the average effective refractive index value, and are listed in Table 4.20.

Table 4.20: Refractive Index Values for Spherical Pores

Sample Name	Porosity (%)	Effective n_o	Effective n_e	Average effective n
BQ0423-15#3	39 ± 8	2.1 ± 0.1	2.1 ± 0.1	2.1 ± 0.1
BQ0423-15#4	56 ± 11	1.8 ± 0.2	1.8 ± 0.2	1.8 ± 0.2
BQ0423-15#5	58 ± 12	1.8 ± 0.2	1.8 ± 0.2	1.8 ± 0.2
BQ0423-15#6	30 ± 6	2.2 ± 0.1	2.2 ± 0.1	2.2 ± 0.1
BQ0423-15#9	35 ± 7	2.1 ± 0.1	2.1 ± 0.1	2.1 ± 0.1
BQ0423-15#10	57 ± 11	1.8 ± 0.2	1.8 ± 0.2	1.8 ± 0.2

The effective n_o and n_e values agree with each other, therefore the average effective n value was used. Using the average refractive index values, the bulk frequency shift values that were determined for each sample, and Equation (2.6), the bulk mode velocities for each sample, assuming spherical pores, were determined and listed in Table 4.21. It was expected that there would be up to two transverse bulk modes and one longitudinal mode per sample but it was found that there were between four and five modes for each sample. Some of these modes had to be ruled out to try and determine which ones were transverse bulk modes and which ones were longitudinal bulk modes. A number of modes can be immediately excluded because, in the case of isotropic materials, the velocity of the slowest bulk mode must be greater than the velocity of the Rayleigh surface mode [35]. From the remaining modes, the mode with the lowest velocity from each sample has been classified as the transverse bulk mode

Table 4.21: Porous SiC Bulk Mode Velocities for Spherical Pores

Sample Name	Porosity (%)	Frequency Shift ($\pm$0.2 GHz)	Velocity ($\times 10^3$ m/s)
BQ0423-15#3	39 ± 8	25.5	3.2 ± 0.2
		32.7	4.1 ± 0.2
		40.6	5.1 ± 0.3
		57.5	7.3 ± 0.4
		69.0	8.7 ± 0.4
BQ0423-15#4	56 ± 11	12.1	1.8 ± 0.2
		20.9	3.1 ± 0.3
		37.0	5.5 ± 0.6
		61.3	9.1 ± 1.0
BQ0423-15#5	58 ± 12	10.3	1.5 ± 0.2
		18.1	2.7 ± 0.3
		25.5	3.8 ± 0.4
		46.5	6.9 ± 0.8
		61.5	9.1 ± 1.0
BQ0423-15#6	30 ± 6	9.5	1.2 ± 0.1
		21.2	2.6 ± 0.1
		29.2	3.5 ± 0.2
		43.7	5.3 ± 0.2
		80.3	9.7 ± 0.4
BQ0423-15#9	35 ± 7	10.5	1.3 ± 0.1
		18.3	2.3 ± 0.1
		25.6	3.2 ± 0.2
		44.2	5.6 ± 0.3
		79.5	10.1 ± 0.5
BQ0423-15#10	57 ± 11	19.1	2.8 ± 0.3
		31.6	4.7 ± 0.5
		58.0	8.6 ± 1.0
		67.3	10.0 ± 1.1

(recall that the frequency shift of the peaks associated with these modes is approximately independent of θ_i). Figure 4.38 is a graph that shows the slow transverse, fast transverse and longitudinal bulk wave velocities as a function of porosity for 6H-SiC for spherical pore shapes ($\xi = 1$) and for a direction of propagation that is at an angle $\theta = 25°$ from the c-axis and was provided by Dr. Devaty and coworkers. The transverse and longitudinal bulk wave velocities that were experimentally determined are also presented in Figure 4.38. It should be noted that there was no easy way to

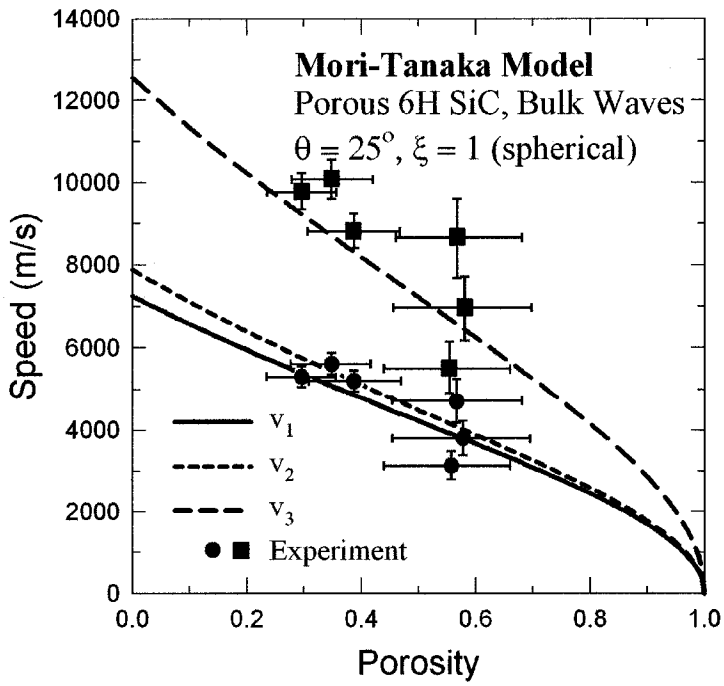

Figure 4.38: Mori-Tanaka model of bulk wave velocities for spherical pore shapes ($\xi = 1$) where v_1 is the slow transverse wave velocity, v_2 is the fast transverse wave velocity, v_3 is the longitudinal wave velocity, • is the transverse mode experimental data, ■ is the longitudinal mode experimental data, and $\theta = 25°$ is the angle that the direction of propagation has with the c-axis.

determine which modes represent the longitudinal bulk modes therefore the modes that most closely agreed with the theoretical curve were used. In every sample, except for BQ0423-15#3, the mode with the next highest velocity, when compared to the transverse bulk mode velocity, was classified as the longitudinal bulk mode. In the case of BQ0423-15#3 the mode with the highest velocity was used. It should be noted that there can be two transverse bulk modes found in a sample but in the case of the PSC samples there was only one found, implying that the two transverse modes have nearly identical velocities. The transverse and longitudinal bulk mode velocities are listed in Table 4.22.

Table 4.22: Transverse and Longitudinal Bulk Mode Velocities for Spherical Pores

Sample Name	Porosity (%)	Bulk Wave Velocity ($\times 10^3$ m/s)	
		Transverse Mode	Longitudinal Mode
BQ0423-15#3	39 ± 8	5.1 ± 0.3	8.7 ± 0.4
BQ0423-15#4	56 ± 11	3.1 ± 0.3	5.5 ± 0.6
BQ0423-15#5	58 ± 12	3.8 ± 0.4	6.9 ± 0.8
BQ0423-15#6	30 ± 6	5.3 ± 0.2	9.7 ± 0.4
BQ0423-15#9	35 ± 7	5.6 ± 0.3	10.1 ± 0.5
BQ0423-15#10	57 ± 11	4.7 ± 0.5	8.6 ± 1.0

It can be seen in Figure 4.38 that the velocities for both the transverse and longitudinal bulk waves agree fairly well with the Mori-Tanaka model for spherical shaped pores. For the transverse bulk mode (• in Figure 4.38), four of the velocities agree very closely with the theoretical curve, while one velocity is slightly higher than the curve and one velocity is slightly lower than the curve. For the longitudinal bulk

mode (■ in Figure 4.38), all of the velocities are higher than, but close to, the theoretical curve while one velocity is lower than the curve. The two velocities that are lower than their respective theoretical curves are from sample BQ0423-15#4, which had a very long etch of $\sim$ 72 hours in 50% HCl that could have increased its porosity, thereby lowering the bulk velocities. There are a number of possibilities as to why some of the remaining velocities do not fall on the theoretical curves. The first possibility is that the 20% uncertainty associated with the porosities of the samples could mean that the reported values for porosity may not be the true values. The next possibility is that the long etch which sample BQ0423-15#4 received altered its porosity. The final possibility is that the theoretical curves in Figure 4.38 are calculated assuming that the direction of propagation has an angle $\theta = 25°$ with the c-axis, whereas the frequency shifts that were used to determine the velocities were obtained by averaging the frequency shifts obtained at an angle of incidence of 30° and 60°. These angles of incidence probe bulk modes that propagate with angles of around 14° and 26° (depending on the sample) respectively, when compared to the c-axis. Therefore, the theoretical model would not be expected to agree completely with the experimental data because of the difference in propagation direction.

Similar to above, Equation (4.3) was used along with the ordinary and extraordinary refractive index values for SiC, the shape factor of 0.2 for prolate spheroid pore shapes, and the appropriate depolarization factors, to find the effective refractive index values for each sample. The average effective refractive index values were also

determined and are listed in Table 4.23. The effective n_o and n_e values agree within their uncertainties, therefore the average effective n value was used for simplicity.

Table 4.23: Refractive Index Values for Prolate Spheroid Shaped Pores

Sample Name	Porosity (%)	Effective n_o	Effective n_e	Average effective n
BQ0423-15#3	39 ± 8	2.0 ± 0.1	2.2 ± 0.1	2.1 ± 0.1
BQ0423-15#4	56 ± 11	1.7 ± 0.2	1.9 ± 0.2	1.8 ± 0.2
BQ0423-15#5	58 ± 12	1.7 ± 0.2	1.9 ± 0.2	1.8 ± 0.2
BQ0423-15#6	30 ± 6	2.1 ± 0.1	2.3 ± 0.1	2.2 ± 0.1
BQ0423-15#9	35 ± 7	2.1 ± 0.1	2.3 ± 0.1	2.2 ± 0.1
BQ0423-15#10	57 ± 11	1.7 ± 0.2	1.9 ± 0.2	1.8 ± 0.2

Using the frequency shifts of the transverse and longitudinal bulk waves as well as the average refractive index values found in Table 4.23 the bulk velocities for prolate spheroid shaped pores were determined and are summarized in Table 4.24.

Table 4.24: Transverse and Longitudinal Bulk Mode Velocities for Prolate Spheroid Shaped Pores

Sample Name	Porosity (%)	Bulk Wave Velocity ($\times 10^3$ m/s)	
		Transverse Mode	Longitudinal Mode
BQ0423-15#3	39 ± 8	5.1 ± 0.3	8.7 ± 0.4
BQ0423-15#4	56 ± 11	3.1 ± 0.3	5.5 ± 0.6
BQ0423-15#5	58 ± 12	3.8 ± 0.4	6.9 ± 0.8
BQ0423-15#6	30 ± 6	5.3 ± 0.2	9.7 ± 0.4
BQ0423-15#9	35 ± 7	5.3 ± 0.2	9.6 ± 0.4
BQ0423-15#10	57 ± 11	4.7 ± 0.5	8.6 ± 1.0

Figure 4.39 is a graph that shows the slow transverse, fast transverse and longitudinal bulk wave velocities as a function of porosity for 6H-SiC for prolate spheroid pore

shapes ($\xi = 0.2$) and for a direction of propagation that is at an angle $\theta = 25°$ from the c-axis and was provided by Devaty and coworkers. The transverse and longitudinal bulk wave velocities that were experimentally determined are also presented in Figure 4.39. It can be seen that the velocities for both the transverse and longitudinal bulk

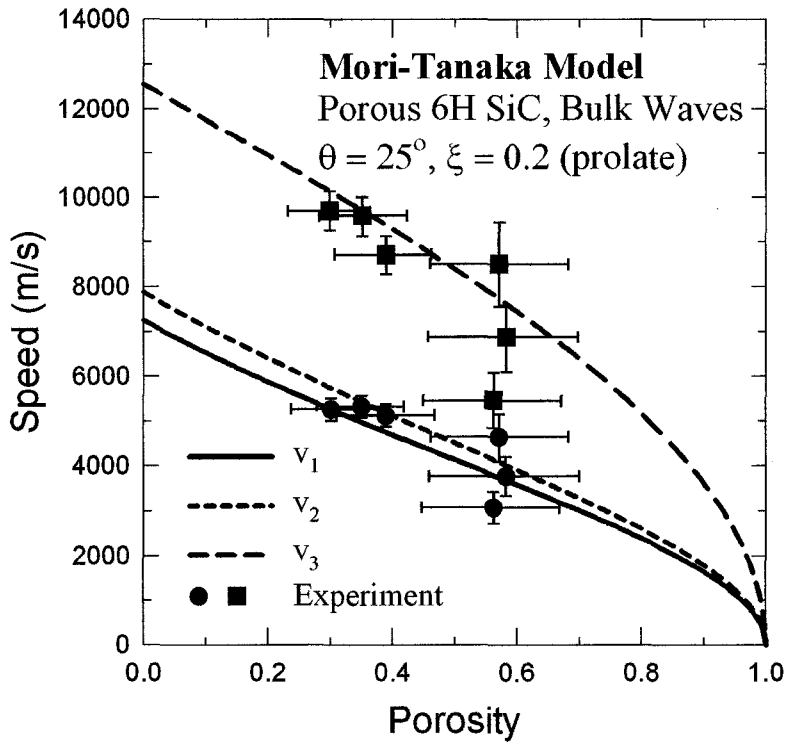

Figure 4.39: Mori Tanaka model of bulk wave velocities for prolate spheroid pore shapes ($\xi = 0.2$) where v_1 is the slow transverse wave velocity, v_2 is the fast transverse wave velocity, v_3 is the longitudinal wave velocity, • is the transverse mode experimental data, ■ is the longitudinal mode experimental data, and $\theta = 25°$ is the angle that the direction of propagation has with the c-axis.

waves agree very well with the Mori-Tanaka model for prolate spheroid shaped pores. For the transverse bulk mode (• in Figure 4.39), four of the velocities agree very closely

with the theoretical curve, while one velocity is slightly higher than the theoretical curve and one velocity is slightly lower than the theoretical curve. For the longitudinal bulk mode (■ in Figure 4.39), one of the velocities agrees with the theoretical curve, three of the velocities are slightly lower than the curve, one velocity is significantly lower than the curve and one velocity is slightly higher than the curve. It can be seen by comparing Figures 4.38 and 4.39 that the experimental data for the acoustic bulk mode velocities agrees the closest with the Mori-Tanaka model when the pores are modeled as having a prolate spheroid shape. Therefore the values in Table 4.24 are taken as the correct values for the transverse and longitudinal bulk mode velocities.

Substrate Bulk Modes

For each sample there were three peaks discovered in the spectra that were taken at an FSR of approximately 125 GHz which are believed to have originated from the SiC substrate of the samples. These peaks are able to be detected due to the optical transparency of the samples. Averaging the peak positions from all of the spectra provides peak positions of 72.8 GHz, 75.9 GHz, and 129.5 GHz. These peaks correspond to the slow transverse, the fast transverse, and the longitudinal modes of the crystalline SiC substrate respectively. Using these frequency shifts, the average value of n_o and n_e for SiC (2.69 ± 0.04), and Equation (2.6), the velocity values for these modes were determined and are summarized in Table 4.25.

Table 4.25: SiC Substrate Bulk Mode Velocities

Mode	Frequency Shift (±0.2 GHz)	Velocity ($\times 10^3$ m/s)
Slow Transverse	72.8	7.2 ± 0.1
Fast Transverse	75.9	7.5 ± 0.1
Longitudinal	129.5	12.8 ± 0.2

According to [18], the velocities for the mixed transverse and longitudinal modes, v_+ and v_- respectively, can be determined from the elastic constants of the material, the angle between the c-axis and the propagation direction of the phonon, and the density of the material. It was found that

$$\begin{aligned} v_{\pm}(\theta) \;=\; & \frac{1}{\sqrt{\rho}}\Bigg\{\frac{1}{2}\left(C_{44}+C_{11}\sin^2\theta+C_{33}\cos^2\theta\right) \\ & \pm\frac{1}{2}\Big[\left(C_{44}+C_{11}\sin^2\theta-C_{33}\cos^2\theta\right)^2 \\ & -4C_{44}\left(C_{11}\sin^2\theta-C_{33}\cos^2\theta\right)\sin^2\theta \\ & +C_{13}\left(C_{13}+2C_{44}\right)\sin^2 2\theta\Big]^{1/2}\Bigg\}^{1/2}, \end{aligned}$$

where C_{11}, C_{13}, C_{33}, and C_{44} are elastic constants of the material, ρ is the density of the material, and θ is the angle between the c-axis and the propagation direction of the phonon. For 6H SiC, $\rho = 3.22\ g/cm^3$, $C_{11} = 501\ GPa$, $C_{13} = 52\ GPa$, $C_{33} = 553\ GPa$, and $G_{44} = 163\ GPa$ [18]. Using these values, along with various θ values, a minimum and maximum value for the mixed transverse and mixed longitudinal modes were able to be found. The transverse bulk mode velocity can range from 7.1×10^3 m/s to 8.6×10^3 m/s while the longitudinal bulk mode velocity can range from 11.8×10^3 m/s to 13.1×10^3 m/s. The experimental values of the transverse and longitudinal

bulk modes both fall within the calculated ranges of allowed velocities implying that these peaks were in fact due to bulk modes from the SiC sample substrate.

Chapter 5

Conclusion

Brillouin spectroscopy was used to study acoustic modes in PSC samples with varying porosities. Initially the samples were coated with a 40 nm layer of aluminum. For each sample there were two peaks whose frequency shift increased with increasing angle of incidence but were determined not to be due to Rayleigh surface modes. There are also between one and three peaks that were due to bulk modes found in each sample and these peaks were ignored because the bulk peaks were found in the spectra taken after the aluminum had been removed. Four of the samples were studied in air while BQ0423-15#5 and BQ0423-15#10 were studied in a near vacuum environment. It was found that the only significant difference between a spectrum taken in air and a spectrum taken at near vacuum is that the background level is greater with the latter case. The samples were then subjected to an acid etch in 50% HCl to remove the aluminum coating. It was found that a 10 minute etch should be sufficient to remove all of the aluminum for the samples. Each sample was found

to have a peak that corresponded with a Rayleigh surface mode and the velocities of this mode ranged from 2.8×10^3 m/s to 5.2×10^3 m/s. In every sample, except for BQ0423-15#4 and BQ0423-15#6, there was a second peak found that behaved similarly to a Rayleigh surface mode but there can only be one Rayleigh surface mode per sample. It is possible that this peak is due to a pseudo-surface mode and it was found to have velocities ranging from 4.6×10^3 m/s to 8.4×10^3 m/s.

Rayleigh surface wave velocities were compared to those theoretically determined by using the Mori-Tanaka acoustic effective medium model. There was reasonable agreement between the theoretical curves for spherical and prolate spheroid pore shapes and the experimentally determined velocities. The variation of the points from the curve can be contributed to the large uncertainty associated with the porosity of the samples. In the case of BQ0423-15#4, the variation from the theoretical curve can be due to the long etch of $\sim$ 72 hours in 50% HCl that the sample received which may have altered its porosity.

There were also between seven and eight possible bulk peaks found for each sample. The Maxwell-Garnett effective dielectric approximation was used to determine the effective refractive index values for the porous layer of each sample, from which bulk mode velocities could be determined. The refractive index values, and therefore the bulk mode velocities, were determined for both spherical and prolate spheroid pore shapes. These velocities were then compared to those theoretically determined by using the Mori-Tanaka acoustic effective medium model for their respective pore

shapes. There was reasonable agreement between the theoretical curves and the experimentally determined velocities for the spherical pore shape while there was a very good agreement between the theoretical curves and the experimentally determined velocities for the prolate spheroid pore shape. Based on the refractive index value for the prolate spheroid pore shape, each sample was found to have a transverse bulk mode which had a velocity ranging between 3.1×10^3 m/s and 5.3×10^3 m/s and a longitudinal bulk mode which had a velocity ranging between 5.5×10^3 m/s to 9.7×10^3 m/s. The variation of the points from the curve can be attributed to the large uncertainty associated with the porosity of the samples. In the case of BQ0423-15#4, the variation from the theoretical curve can be due to the long etch that the sample received which may have altered its porosity. Also it should be noted that the Mori-Tanaka model for the bulk modes is based on a propagation direction that has an angle of 25° when compared to the c-axis, while the experimental data was determined by averaging the frequency shifts from spectra that probed phonons that were propagating with angles of 14° and 26°. This means that the experimental data would not be expected to agree exactly with the theoretical curve, thereby allowing for some of the variation between the data and the theoretical curve.

Three of the bulk peaks from each sample are due to the SiC substrate of the samples. The average velocities for these peaks were determined to be 7.2×10^3 m/s, 7.5×10^3 m/s, and 12.8×10^3 m/s. Using an equation that related the mixed transverse and longitudinal bulk wave velocities to the samples elastic constants, density, and the

propagation direction of the wave compared to the c-axis, a range of possible velocities was determined for the substrate. For the mixed transverse bulk wave the possible velocities ranged between 7.1×10^3 m/s and 8.6×10^3 m/s. The first two velocities fall within this range implying they represent the slow and fast transverse bulk modes of the substrate. For the mixed longitudinal bulk wave the possible velocities ranged between 11.8×10^3 m/s and 13.1×10^3 m/s. The last velocity falls within this range implying that it is the longitudinal bulk mode for the substrate.

The data presented here is the first step in determining some of the physical properties of PSC. Further study would allow for a determination of the elastic constants of the PSC layers. The collected data can be beneficial in determining a more appropriate value for the shape factor in the Mori-Tanaka acoustic effective medium model for the particular samples studied. There is also the opportunity that Brillouin scattering in combination with the acoustic effective medium model could be used as a probe to determine a sample's pore shape.

Bibliography

[1] F. Ren and J. C. Zolper, editors, *Wide Energy Bandgap Electronic Devices* (World Scientific Publishing Co. Pte. Ltd., 2003).

[2] W. J. Choyke, H. Matsunami and G. Pensl, editors, *Silicon Carbide: Recent Major Advances* (Springer-Verlag, 2004).

[3] S. Elliott, *The Physics and Chemistry of Solids* (John Wiley & Sons Ltd., 1998).

[4] P. Djemia, Y. Roussigné, G. F. Dirras and K. M. Jackson, J. Appl. Phys. **95**, 2324 (2004).

[5] K. A. Jackson and W. Schröter, editors*Handbook of Semiconductor Technology* Vol. 1 (Wiley-VCH, 2000).

[6] S. Zangooie and H. Arwin, J. Electrochem. Soc. **148**, G297 (2001).

[7] J. S. Shor, L. Bemis, A. D. Kurtz, I. Grimberg, B. Z. Weiss, M. F. MacMillian and W. J. Choyke, J. Appl. Phys. **76**, 4045 (1994).

[8] Y. Shishkin, Y. Ke, R. P. Devaty and W. J. Choyke, J. Appl. Phys. **97**, 44908 (2005).

[9] O. Jessensky, F. Müller and U. Gösele, Thin Solid Films **297**, 224 (1997).

[10] F. Hassen, R. M'Ghaieth, H. Maaref and R. Madar, Mater. Sci. Eng., C **15**, 113 (2001).

[11] A. O. Konstantinov, C. I. Harris and E. Janzén, Appl. Phys. Lett. **65**, 2699 (1994).

[12] W. Shin, W. Seo and K. Koumoto, J. Aust. Ceramic Soc. **33**, 38 (1997).

[13] L. M. Sorokin, N. S. Savkina, V. B. Shuman, A. A. Lebedev, G. N. Mosina and G. Hutchison, Tech. Phys. Lett. **28**, 935 (2002).

[14] A. O. Konstantinov, C. I. Harris, A. Henry and E. Janzén, Inst. Phys. Conf. Ser. **142**, 1079 (1996).

[15] Y. Shishkin, W. J. Choyke and R. P. Devaty, Mater. Sci. Forum **457-460**, 1467 (2004).

[16] M. Matsukawa, S. Murata, T. Matsumoto, T. Matsutani and M. Kiuchi, Ultrasonics **42**, 391 (2004).

[17] S. Murata, M. Matsukawa, T. Matsumoto, S. Sugimoto, S. Goto, M. Kiuchi and N. Ohtori, Jpn. J. Appl. Phys. **41**, 3374 (2002).

[18] K. Kamitani, M. Grimsditch, J. C. Nipko, C. K. Loong, M. Okada and I. Kimura, J. Appl. Phys. **82**, 3152 (1997).

[19] G. T. Andrews, M. J. Clouter, B. Mroz, Y. Shishkin, Y. Ke, R. P. Devaty and W. J. Choyke, Mater. Sci. Forum **457-460**, 653 (2004).

[20] M. J. Damzen, V. I. Vlad, V. Babin and A. Mocofanescu, *Stimulated Brillouin Scattering: Fundamentals and Applications* (IOP Publishing Ltd., 2003).

[21] S. F. Ahmad, H. Kiefte, M. J. Clouter and M. D. Whitmore, Phys. Rev. B: Condens. Matter **26**, 4239 (1982).

[22] K. D. Möller, *Optics* (University Science Books, 1988).

[23] R. Loudon and J. R. Sandercock, J. Phys. C **13**, 1609 (1980).

[24] A. Anderson, editor, *The Raman Effect* (Marcel Dekker, Inc., 1971).

[25] D. C. Gazis, R. Herman and R. F. Wallis, Phys. Rev. **119**, 533 (1960).

[26] J. R. Sandercock, Solid State Commun. **26**, 547 (1978).

[27] S. F. Jacobs, M. Sargent III, J. F. Scott and M. O. Scully, editors*Physics of Quantum Electronics: Laser Applications to Optics and Spectroscopy* Vol. 2 (Addison-Wesley Publishing Company, 1975).

[28] J. A. Gonzalo, J. de Frutos and J. García, *Solid State Spectroscopies: Basic Principles and Applications* (World Scientific Publishing Co. Pte. Ltd., 2002).

[29] W. Demtröder, *Laser Spectroscopy: Basic Concepts and Instrumentation*, Second ed. (Springer-Verlag, 1996).

[30] B. Chu, *Laser Light Scattering: Basic Principles and Practice*, Second ed. (Academic Press, Inc., 1991).

[31] R. Pecora, editor, *Dynamic Light Scattering: Applications of Photon Correlation Spectroscopy* (Plenum Press, 1985).

[32] J. R. Sandercock, *Tandem Fabry-Perot Interferometer TFP-1*, JRS Scientific Instruments, CH-8909 Zwillikon, Switzerland, 2001.

[33] R. F. Wallis and G. I. Stegeman, editors, *Electromagnetic Surface Excitations* (Springer-Verlag, 1986).

[34] Y. Bogumilowicz, J. M. Hartmann, R. Truche, Y. Campidelli, G. Rolland and T. Billon, Semicond. Sci. Technol. **20**, 127 (2005).

[35] A. A. Oliner, editor*Acoustic Surface Waves* Vol. 24 (Springer-Verlag, 1978).

[36] T. Mori and K. Tanaka, Acta Metall. **21**, 571 (1973).

[37] L. D. Landau and E. M. Lifshitz, *Electrodynamics of Continuous Media* (Pergamon Press Ltd., 1960).

[38] M. M. Seikh, C. Narayana, S. Parashar and A. K. Sood, Solid State Commun. **127**, 209 (2003).

[39] R. E. Camley and F. Nizzoli, J. Phys. C **18**, 4795 (1985).

[40] P. T. B. Shaffer, Appl. Opt. **10**, 1034 (1971).

[41] R. P. Devaty and A. J. Sievers, Phys. Rev. B **31**, 2427 (1985).